Ocean Engineering 311 (2024) 118905

Contents lists available at ScienceDirect

Ocean Engineering

journal homepage: www.elsevier.com/locate/oceaneng

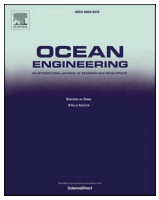

Research paper

Development and prediction of scour around offshore wind turbine monopile foundations in ebb and flow tides

Fei Geng [a], Wenxian Yang [b,*], Sadegh Nadimi [a], Zhiqiang Hu [a]

[a] School of Engineering, Newcastle University, Newcastle Upon Tyne, NE1 7RU, UK
[b] School of Computing and Engineering, University of Huddersfield, Huddersfield, HD1 3DH, UK

ARTICLE INFO

Keywords:
Offshore wind
Ebb and flow
Monopile
Scour

ABSTRACT

Monopile foundations are commonly used to support offshore wind turbines (OWTs) in nearshore shallow waters, where the periodic ebb and flow of tides can cause severe seabed erosion around these foundations. Accurately predicting the progression of scour depth under these tidal conditions is crucial for the safety of OWTs. While a few empirical formulas for equilibrium scour depth in periodic tides have been proposed, they often overlook the backfilling effects during their derivation. Consequently, these methods fail to predict the progression of scour depth characterized by recurring scouring and backfilling processes. In this study, the scour progression under different tidal patterns, including square tides, symmetrical sinusoidal tides, and asymmetrical sinusoidal tides with various periods, is investigated using numerical methods. It is indicated by the results that deeper scour depths are produced by symmetrical tides compared to asymmetrical tides, while the highest scour depth is observed under square tides, potentially slightly exceeding that under unidirectional currents. Additionally, asymmetric scour depths at the front and back sides of the pile can result from the asymmetry of tides. Although scour progression is affected by tide periods, their impact on the equilibrium scour depth is limited. Furthermore, a new concept called normalized cumulative effective flow intensity is introduced, which plays a primary role in governing equilibrium scour depth. Based on this concept, prediction methods for both equilibrium scour depth and scour progression under sinusoidal tides, which closely resemble natural tidal patterns, are proposed. The accuracy of these methods is validated by experimental data from previous studies. These findings not only provide a method to optimize the design of monopile burial depth but also aid in the development of appropriate maintenance measures to prevent scour-induced damage to OWT foundations over their long lifespans.

1. Introduction

With offshore wind turbines (OWTs) proliferating around the world, offshore wind power has emerged as a potent and efficient solution to tackle the pressing issue of climate change (Gunnar, 2022). Attribute to mature technology, low cost and easy installation, bottom fixed foundations are currently the primary type of foundations used in the offshore wind industry, with monopile foundations being the most widely adopted (Lee and Zhao, 2021; Geng et al., 2023). To date, more than 75% of OWTs are supported by monopiles, particularly in nearshore shallow waters (Dai et al., 2021). However, in these areas, the repetitive ebb and flow of tides can cause significant scour around the monopile foundations, posing a major threat to the safety of OWTs (Whitehouse et al., 2011).

Over the past decades, extensive studies have been conducted in bridge engineering to understand scour around bridge piles (Melville and Raudkivi, 1977; Roulund et al., 2005; Chreties et al., 2013). However, the knowledge gained from these studies is still not sufficient enough to fully explain scour around OWT monopile foundations due to the significant differences between the two application scenarios. Therefore, targeted research that considers the actual offshore environments where OWTs operate is still necessary to understand the scour of OWT monopiles. To meet this need, many studies have investigated the scour of OWT foundations in pure currents (e.g. Yang et al., 2021a), pure waves (e.g. Carreiras et al., 2012), and under combined wave-current conditions (Petersen et al., 2012; Ong et al., 2013; Qi and Gao, 2014a, 2014b; Qin et al., 2023). By contrast, research into the scour of OWT monopiles caused by periodic tidal ebb and flow remains very

* Corresponding author.
E-mail address: w.yang@hud.ac.uk (W. Yang).

https://doi.org/10.1016/j.oceaneng.2024.118905
Received 3 June 2024; Received in revised form 8 July 2024; Accepted 3 August 2024
Available online 17 August 2024

limited, with only a few exceptions.

There is a significant difference between the evolution mechanisms of scour holes caused by periodic tides and those produced by unidirectional currents. In unidirectional currents, the maximum scour depth around a pile typically occurs on the upstream side. However, under periodic tidal action, it can occur on both the front and back sides due to the periodic reversal of flow direction (Escarameia and May 1999). Alongside the scouring process on the upstream side, a backfilling process occurs on the downstream side, alternating between the front and back sides of the pile in response to the changing tidal flow direction (Jensen et al., 2006).

To investigate these phenomena, different simplified methods have been applied in both experimental and numerical studies. A commonly adopted approach assumes that both water depth and current velocity magnitude remain constant while periodically reversing the flow direction (Escarameia and May, 1999; Margheritini et al., 2007; Whitehouse and Stroescu, 2023). This flow velocity pattern is referred to as a square tide (Yao et al., 2016). To investigate the effects of variations in velocity and water depth, the signals of current velocity and water depth in each tide cycle were discretized into several sections with different values in the experiments by McGovern et al. (2014). More recently, some studies (Porter et al., 2014; Schendel et al., 2019; Yang et al., 2021b; Wang et al., 2024) have conducted simulations using sinusoidal tides, where the current velocity varies in a sinusoidal pattern while the water depth remains constant. Additionally, Schendel et al. (2018) utilized an onsite-measured tide-induced current velocity signal in their experiments, which closely resembles a sinusoidal signal.

These studies have reported significant differences in scour progressions under unidirectional currents compared to periodic tides. Generally, with a square tide, the scour depth increases more rapidly under periodic tides than under corresponding unidirectional currents. Conversely, when considering time-varying tidal velocities, periodic tides consistently result in slower scour progression and smaller scour depths compared to unidirectional currents with velocities equivalent to the peak velocity of the tides.

Due to the gradually changing terrain in nearby coastal areas, as well as the interplay between the asymmetry effects of astronomical forces and the nonlinear interactions of tides and currents (Zhang et al., 2018), a remarkable uneven pattern between the ebb and flow of tides can occur under specific conditions, affecting scour progression. Although an onsite-measured tide signal was considered in experiment by Schendel et al. (2018), the effect of ebb and flow asymmetry on scour progression was not investigated. Regarding the impact of tide periods, Whitehouse and Stroescu (2023) conducted experiments on scour under square tides with varying tide periods and found that tide periods have a key controlling effect on scour depth over a fixed number of tide cycles. This finding was expected, but since the number of cycles was fixed, the total scour time varied significantly across cases. It is anticipated that longer scour times will result in deeper scour depths. However, for engineering practice, it is more crucial to understand how tide periods affect equilibrium scour depth, scour pit morphology, and time scales. This is why this study will focus on investigating these questions, providing insights into predicting scour progression under periodic tides.

In terms of predicting scour depth in periodic tides, several efforts have been made. Although some prediction methods recommended by standards (Richardson and Davis, 1995; MTPRC, 2015; DNV, 2016) are widely applied in engineering practice, they have proven to be inapplicable to tidal scenarios (Schendel et al., 2018) because most of these methods were derived from scour data in unidirectional currents. Schendel et al. (2018) conducted scour tests using sinusoidal-like tides and introduced two characteristic velocities for sinusoidal tides: peak velocity U_{max} and root mean square velocity U_{rms}. The results showed that the equilibrium scour depth for a unidirectional current with a velocity of U_{max} is higher than that of the corresponding sinusoidal tide, while a unidirectional current with a velocity of U_{rms} results in a shallower scour pit than the corresponding sinusoidal tide. Based on this observation, they recommended using a current velocity 15%–25% higher than U_{rms} to estimate the scour depth of corresponding sinusoidal tides, indicating that an appropriate equivalent velocity is essential for this estimation. Wang et al. (2024) proposed an empirical equation to calculate the equivalent velocity between sinusoidal and square tides, providing a way to simplify the sinusoidal tidal signal to a square tide signal. However, there remains a significant difference between the scour depth caused by unidirectional currents and square tides, making it inappropriate to directly extend the scour depth prediction methods for unidirectional currents to periodic tides. Considering the periodic scouring and interval process under sinusoidal tides, Schendel et al. (2019) introduced the concept of effective flow work (Link et al., 2017; Pizarro et al., 2017) which refers to the work of flow imposed on the sediment during periods when the current velocity exceeds a predefined critical value. They proposed an empirical equation relating effective flow work to equilibrium scour depth, which can be used to predict equilibrium scour depth in periodic tides. This method was further verified by experimental results for both square and sinusoidal tides with various flow velocities (Whitehouse and Stroescu, 2023; Wang et al., 2024). However, both sinusoidal and square tides considered in these studies are symmetrical. Whether this method can be applied to asymmetric tides, characterized by uneven peak velocities during ebb and flow, remains unclear. Additionally, all effective periods with flow velocities higher than the critical value were included in the calculation of effective flow work, which is positively correlated with equilibrium scour depth. This approach may cause theoretical confusion, as some effective periods may only contribute to backfilling effects on the scour pit, which are theoretically negatively correlated with scour depth. Consequently, this method cannot be applied to predict the progression of tide-induced scour depth development (Schendel et al., 2019), characterized by a repeating scour-backfilling process.

To explore a potential solution for this issue, scour progression under square tides, symmetrical sinusoidal tides, and asymmetrical sinusoidal tides with various tide periods is investigated in this paper using numerical methods. Based on data analysis, a new concept called normalized cumulative effective flow intensity is proposed to predict equilibrium scour depths and scour progression in sinusoidal tides, which closely resemble natural tides. The accuracy of this newly proposed method is verified using experimental data from previous studies, demonstrating high prediction accuracy.

2. Numerical model

2.1. Governing equations

The scour simulation is conducted using the FLOW3D-HYDRO (V2022) software, which employs a sediment scour model to simulate the scour process. In this model, sediment transport is characterized by two states: suspended and packed. Suspended sediment is modelled as sediment concentration in the fluid and converts to packed sediment once it reaches the critical packing fraction, typically suggested to be 0.64. Sediment transport involves five mechanisms: entrainment, advection, drifting, bed load transport, and packing. Entrainment occurs when packed sediment is picked up due to bed shear stress, transitioning to the suspended state. Conversely, packing is the process where suspended sediment settles and converts back to the packed state. Suspended sediment can either be carried along by fluid flow (advection) or settle due to gravity (drifting). When bed shear stress is insufficient to initiate advection, sediment may roll or bounce along the bed, known as bed load transport.

Due to the computational limitations, it is impracticable to calculate the fluid dynamic of each sediment particle. Instead, an empirical model proposed by Mastbergen and Van Den Berg (2003) is used to implement the entrainment, with the critical Shields parameter serving as the criterion. The dimensionless critical Shields parameter θ_{cr} is calculated

using the formula suggested by Soulsby (1997):

$$\theta_{cr}=\frac{0.3}{1+1.2d_*}+0.055[1-\exp(-0.02d_*)] \tag{1}$$

where d_* is a dimensionless parameter calculated by:

$$d_*=d\left[\frac{\rho(\rho_s-\rho)g}{\mu_f^2}\right]^{\frac{1}{3}} \tag{2}$$

where ρ_s and ρ are density of sediment particle and fluid respectively; d is the diameter of sediment particle; μ_f refers to the dynamic viscosity of fluid; and g is the acceleration of gravity.

The local Shields parameter induced by the bed shear stress can be calculated by:

$$\theta=\frac{\tau}{gd(\rho_s-\rho)} \tag{3}$$

where τ refers to the fluid induced local bed shear stress calculated through the law of the wall.

When $\theta\geq\theta_{cr}$, the entrainment occurred, and the lift velocity of suspended sediment can be calculated by Mastbergen and Van Den Berg (2003):

$$\mathbf{u}_{\text{lift}}=\alpha_i\mathbf{n}_s d_*^{0.3}(\theta-\theta_{cr})^{1.5}\sqrt{\frac{gd(\rho_s-\rho)}{\rho}} \tag{4}$$

where α_i is the entrainment parameter, which is suggested to be 0.018 (Mastbergen and Van Den Berg, 2003); $\mathbf{n_s}$ is the outward pointing normal vector of the bed surface. $\mathbf{u}_{\text{lift}}$ is then applied to calculate the amount of packed sediment that is converted into suspended state.

The settling velocity of suspended sediment induced by the gravity is calculated by:

$$\mathbf{u}_{\text{setting}}=\frac{\nu_f}{d}\left[\left(10.36^2+1.049d_*^3\right)^{0.5}-10.36\right]\frac{\mathbf{g}}{\|\mathbf{g}\|} \tag{5}$$

where ν_f is the kinematic viscosity of fluid. It is assumed that the settling motion is in the gravity direction,

The bed-load transport equation is defined as (Meyer-Peter and Müller, 1948):

$$\Phi=\beta_b(\theta-\theta_{cr})^{1.5} \tag{6}$$

where Φ denotes the dimensionless volumetric transport rate of sediment per width of bed; β_b is a coefficient the recommended value of which is 8.0 (Meyer-Peter and Müller, 1948).

Based on the Φ, the volumetric bed-load transport rate q_b is calculated by:

$$q_b=\Phi\left[\|g\|\left(\frac{\rho_s-\rho}{\rho}\right)d^3\right]^{0.5} \tag{7}$$

Correspondingly, the bed-load velocity is calculated by:

$$u_{bedload}=\frac{q_b}{\delta f_b} \tag{8}$$

where δ is the thickness of the packed sediment; f_b is the critical packing fraction of the sediment. Herein the direction of bed-load velocity is assumed to be as the direction of fluid flow adjacent to the packed bed interface.

The suspended sediment is modelled as a continuous concentration, and value of which is calculated by solving the transport equation of sediment advected with fluid flow:

$$\frac{\partial C_s}{\partial t}+\nabla\cdot(\mathbf{u_s}C_s)=\nabla\cdot\nabla(D_sC_s) \tag{9}$$

where C_s is the mass concentration of suspended sediment in the fluid-sediment mixture; D_s is the diffusivity; $\mathbf{u_s}$ is the suspended sediment velocity. In the simplified scour model, the grains in suspension are assumed to do not have strong interactions with each other, and the settling velocity is assumed to be the only difference between velocity of suspended particles and fluid-sediment mixture. Accordingly, the $\mathbf{u_s}$ is calculated by:

$$\mathbf{u_s}=\overline{\mathbf{u}}+\mathbf{u}_{\text{setting}}\frac{C_s}{\rho} \tag{10}$$

where $\overline{\mathbf{u}}$ is the velocity of the fluid-sediment mixture.

In this study, the fluid is considered as an incompressible viscous fluid, the hydrodynamics of which is solved by the RANS (Reynolds-averaged Navier-Stokes) equations as follows:

$$\frac{\partial u_i}{\partial x_i}=0 \tag{11}$$

$$\frac{\partial u_i}{\partial t}+u_j\frac{\partial u_i}{\partial x_j}=-\frac{1}{\rho}\frac{\partial p}{\partial x_i}+\nu\frac{\partial^2 u_i}{\partial x_i^2}+\frac{\partial \tau_{ij}}{\partial x_j} \tag{12}$$

Where, x_i ($i=1$, 2 and 3) refers to the Cartesian coordinate, u_i denotes the velocity in x_i direction, ν is the kinematic viscosity, p represents the pressure, ρ is the fluid density, t is time, and τ_{ij} refers to the Reynolds stress defied as:

$$\tau_{ij}=\nu_t\left(\frac{\partial u_i}{\partial x_j}+\frac{\partial u_j}{\partial x_i}\right)-\frac{2}{3}\delta_{ij}\kappa \tag{13}$$

where δ_{ij} refers to the Kronecker delta, κ is the turbulent energy, ν_t is the turbulent viscosity.

Considering the reliable performance of the RNG k-ε model in simulating low-turbulence-intensity flows in strong shear regions (Salaheldin et al., 2004), it was recommended for simulating the separated turbulent flow around vertical circular piers in water flow (Yang et al., 2021b), and accordingly, it is adopted in this study. The transport equations of RNG k-ε model are written as follows (Yakhot et al., 1992):

$$\frac{\partial}{\partial t}(\rho k)+\frac{\partial}{\partial x_i}(\rho k u_i)=\frac{\partial}{\partial x_j}\left[\left(\mu+\frac{\mu_t}{\sigma_k}\right)\frac{\partial k}{\partial x_j}\right]+\mu_t S^2-\rho\epsilon \tag{14}$$

$$\frac{\partial}{\partial t}(\rho \epsilon)+\frac{\partial}{\partial x_i}(\rho \epsilon u_i)=\frac{\partial}{\partial x_j}\left[\left(\mu+\frac{\mu_t}{\sigma_\epsilon}\right)\frac{\partial \epsilon}{\partial x_j}\right]+C_{\epsilon 1}\frac{\epsilon}{k}P_k-C_{\epsilon 2}^*\rho\frac{\epsilon^2}{k} \tag{15}$$

where, the coefficient $C_{2\epsilon}^*$ can be calculated by:

$$C_{\epsilon 2}^*=C_{\epsilon 2}+\frac{C_\mu\eta^3(1-\eta/\eta_0)}{1+\beta\eta^3} \tag{16}$$

$$\eta=S\frac{k}{\varepsilon} \tag{17}$$

$$S=\sqrt{2S_{ij}\cdot S_{ij}} \tag{18}$$

The value of coefficients in RNG k-ε model are derived as: $C_\mu=0.0845$; $\sigma_k=0.7194$; $\sigma_\epsilon=0.7194$; $C_{\epsilon 1}=1.42$; $C_{\epsilon 2}=1.68$; $\eta_0=4.38$; $\beta=0.012$.

2.2. Numerical model set-up and scenarios of interests

As Fig. 1 shows, the numerical model consists of a scaled OWT monopile foundation, a sediment region for simulating the seabed in the vicinity of the monopile foundation, and a fluid region for modelling periodic tides. In addition, a pair of baffles with a thickness of 4 cm is respectively placed at the inlet and outlet boundaries of the model to maintain a smooth flow away from the scour region and prevent sediment erosion at both inlet and outlet boundaries of the numerical model. In this study, the Froude number similarity criterion is employed to scale the prototype model. Considering a scaling parameter $\lambda=1:90$, the

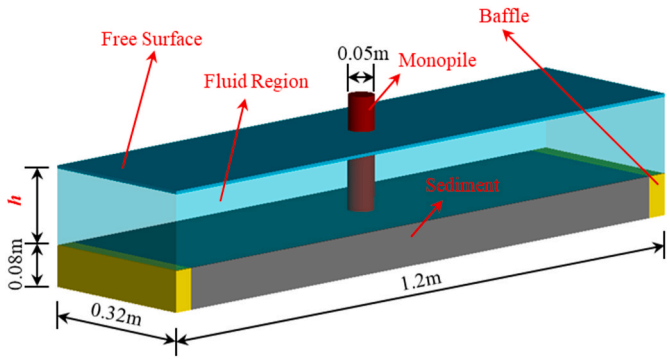

Fig. 1. The numerical model for simulating monopile, periodic tides, and sediment.

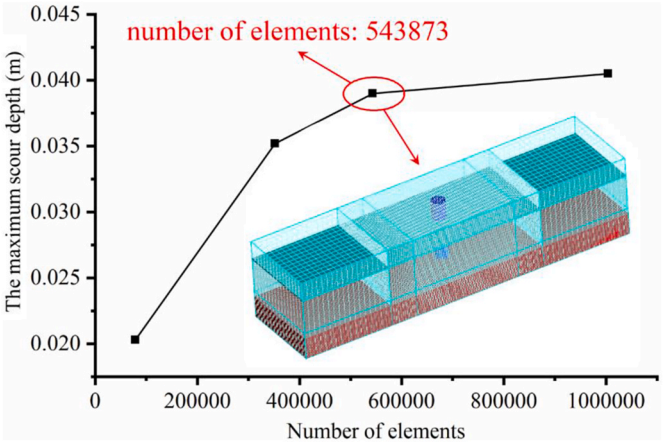

Fig. 2. Convergence analysis of the numerical calculations.

scaled monopile shown in Fig. 1 has a diameter of $D = 0.05$ m, corresponding to the foundation of a 2 MW OWT, such as Siemens Gamesa's SWT-2.3-108 OWT that has a 4.5 m diameter monopile foundation and operates in currents with a speed of 2.3 m/s. In addition, the scaled monopile in the model has a length of 0.3 m, with 0.08 m embedded in the soil. The computational domain of the model has dimensions of 1.2 m (24D) in length, 0.32 m (6.4D) in width, and 0.3 m in height. The sediment area measures 1 m in length, 0.32m in width, and 0.08 m in depth. The sediment is modelled by uniform sand particles with diameter of 0.385 mm and density of 2650 kg/m^3. The surface roughness of the bed and baffles is set equivalent to the diameter of sediment particles (Kadivar et al., 2021). The water depth (h) and flow velocity (U) vary depending on the scenarios.

The inlet boundary on the left side of the numerical model is designated as the 'Velocity Boundary', which is characterised by prescribing the flow velocity in terms of the mean velocity profile and determining the water depth. The outlet boundary on the right side of the model is defined as the 'Pressure Boundary', which specifies the depth of water flowing out of the computational domain. The top boundary is also the 'Pressure Boundary' where the fluid fraction is zero, indicating the presence of a free water surface at the top of the fluid region. The initial elevation of this surface is set to the same value as the water depth. The bottom surface of the computational domain is defined as the 'Wall Boundary', which restricts the flow from penetrating the boundary. Finally, the 'Symmetry Boundary' conditions are applied to the lateral sides of the numerical model to enable frictionless fluid motion along the boundaries while prohibiting inflow or outflow through the boundaries.

The numerical model is divided into three sections for meshing purposes. This partitioning is achieved by two planes, each located 12D away from the pile centre, on the upstream and downstream side of the pile respectively. To ensure accuracy, the central segment, where the scour pit is likely to develop, is intricately meshed with a high level of detail. On the other hand, the remaining two sections located outside the central area are more coarsely meshed with fewer details to conserve computational resources, while still maintaining the stability of the calculations. To guarantee the reliability of the research findings, a convergence analysis was carried out prior to conducting numerical simulations for the study. The aim of the convergence analysis was to determine the optimal mesh size and the number of elements that strike a balance between computational efficiency and precision. In the convergence analysis, the ratio of normal mesh size in the central segment to that in external segments remains at 0.5. Herein, the convergence analysis was performed under the assumption that the scour of the monopile was due to a unidirectional current with a velocity of 0.25 m/s and a water depth of 0.15 m. The maximum scour depth obtained when the scour persisted for 30 min was utilized as the benchmark. Its results obtained when using different numbers of elements are presented in Fig. 2.

From Fig. 2, it is found that a saturated value is essentially obtained for the maximum scour depth once the number of elements reaches 543,873. Therefore, this specific number of elements is selected for meshing the computational domain in the subsequent study. The corresponding normal mesh size in the central and external segments is 1 cm and 2 cm, respectively It should be noted that in the central segment, the mesh size along the flow direction gradually decreases from 1 cm at the border to 0.5 cm at the centre. In the other directions, the mesh is uniformly distributed with the normal size.

Since the inflow boundary is defined by the average flow velocity in the numerical model, the flow velocity profile will vary along the flow direction under the effect of bed friction. The development of flow velocity profiles along the flow direction is illustrated in Fig. 3 (a), where x refers to distance from the inlet boundary along the flow direction, while z represents the distance above the seabed. It shows that the flow velocity is uniformly distributed along the vertical direction at the inlet boundary. However, it gradually decreases near the seabed as the distance from the inlet boundary increases. As x increases, the flow velocity profile transitions from a straight line to a logarithmic curve, stabilizing after reaching 30 cm. The flow region near the bed, where the flow velocity increases gradually with z, is defined as a boundary layer. In this study, a current velocity of 0.25 m/s is used as the criterion to define the boundary layer region and calculate the boundary layer thickness δ. The development of boundary layer thickness with distance from the inlet boundary is plotted in Fig. 3 (b). It shows the boundary layer increases rapidly near the inlet boundary as x increases, and then reaches a stable value of approximately 1.9 cm for $x \geq 30$ cm. It indicates that the distance between inlet boundary and pile, set as 60 cm, is sufficient for the development of flow velocity profile and boundary layer.

Furthermore, to validate the accuracy of the boundary conditions and sediment characteristics used in the numerical model, a comparison is conducted between the 30-min scour progression obtained through numerical calculation and the physical model test results obtained by Melville and Raudkivi (1977). The comparison results are shown in Fig. 4.

The results presented in Fig. 4 indicate a strong agreement between the outcomes of the numerical calculations and the physical model test results, despite minor deviations can be observed. The relative error between the experimental and numerical results at the end of the simulation is less than 5%. Considering the effects of experimental environments and the operational processes, this error is deemed acceptable.

In order to investigate the effects of tide patterns, asymmetry of ebb and flows and tide periods on scour progression and equilibrium scour depth, multiple scenarios characterised by different tide patterns, tide periods, and flow intensities will be considered in the following study. The details about these scenarios are presented in Table 1. In the table, the scenario that considers a unidirectional tidal current (indicated by

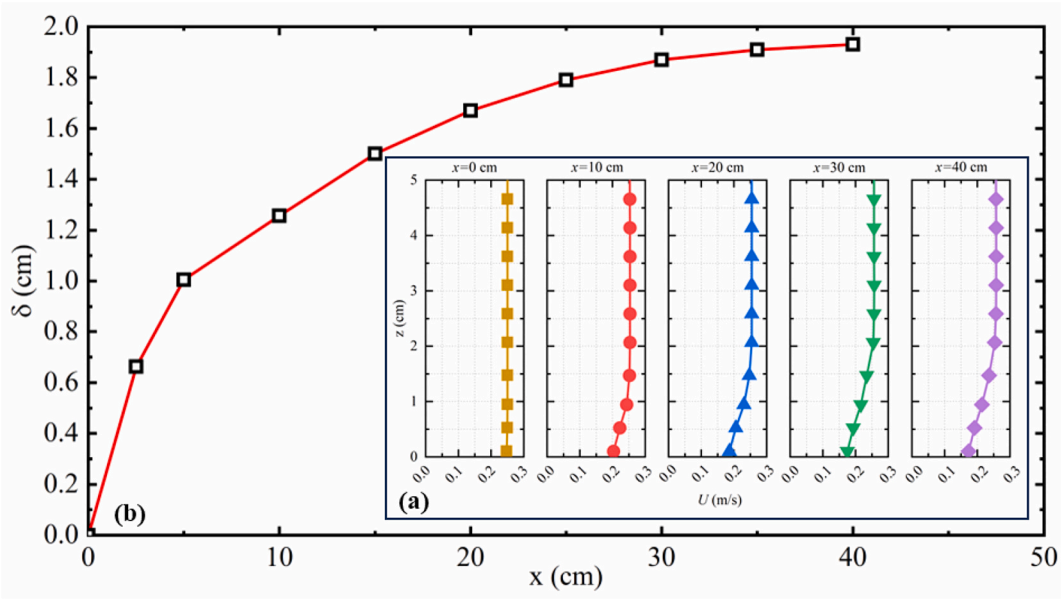

Fig. 3. Verification of the flow velocity profiles. (a) flow velocity profiles at different cross sections. (b) Development of boundary layer depth along flow direction.

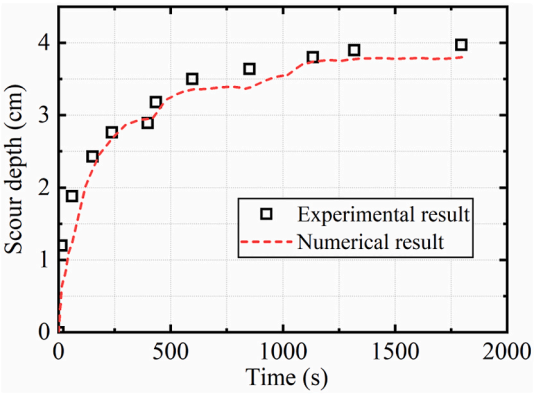

Fig. 4. Verification of the numerical model.

Table 1
Scenarios considered in the study.

Scenarios	Velocity 'U' or Velocity parameters (m/s)	Water depth 'h' or Water depth parameters (m)	Tide period 'T' (min)	Tide pattern
Uni	$U = 0.25$	$h = 0.15$	×	Unidirectional Current
SqT60	$U = 0.25$	$h = 0.15$	60	Square tide
SqT5	$U = 0.25$	$h = 0.15$	5	Square tide
SSinT60	$A = 0.25$, $B = 0$	$C = -0.05$, $D = 0.15$	60	Symmetrical sinusoidal tide
SSinT30	$A = 0.25$, $B = 0$	$C = -0.05$, $D = 0.15$	30	Symmetrical sinusoidal tide
SSinT5	$A = 0.25$, $B = 0$	$C = -0.05$, $D = 0.15$	5	Symmetrical sinusoidal tide
ASinT5	$A = 0.23$, $B = 0.02$	$C = -0.05$, $D = 0.15$	5	Asymmetrical sinusoidal tide
ASinT15	$A = 0.23$, $B = 0.02$	$C = -0.05$, $D = 0.15$	15	Asymmetrical sinusoidal tide
ASinT30	$A = 0.23$, $B = 0.02$	$C = -0.05$, $D = 0.15$	30	Asymmetrical sinusoidal tide
ASinT60	$A = 0.23$, $B = 0.02$	$C = -0.05$, $D = 0.15$	60	Asymmetrical sinusoidal tide
ASinT5R	$A = 0.23$, $B = -0.02$	$C = -0.05$, $D = 0.15$	5	Asymmetrical sinusoidal tide

'Uni') with constant flow velocity and water depth is used as a reference. The abbreviation 'SqTx' refers to 'square tide' scenarios, in which the flow direction reverses periodically with a period of 'x' minutes, but flow velocity and water depth remain constant. The abbreviation 'SSinTx' refers to 'Symmetrical sinusoidal tide' scenarios, in which both flow velocity and water depth vary over time according to a sinusoidal signal. 'ASinTx' refers to the modifications of the corresponding 'SSinTx' scenarios by introducing asymmetry into the tide's ebb and flow. Lastly, to understand the effect of the dominant flow direction on scour, two scenarios, 'ASinT5' and 'ASinT5R' are considered. They have the same tide pattern but different dominant flow directions.

In Table 2, parameters A, B, C, and D are used to define the time-varying flow velocity U and water depth h for symmetrical and asymmetrical sinusoidal tide scenarios, i.e.

$$U(t) = A \sin\left(\frac{2\pi}{T}t\right) + B \tag{19}$$

and

$$h(t) = C \cos\left(\frac{2\pi}{T}t\right) + D \tag{20}$$

where U represents the instantaneous flow velocity, with a positive value indicating a flow towards the right side of the model depicted in Fig. 1, and a negative value representing the opposite direction; A is the oscillating amplitude of the flow velocity; T denotes the period of tide; B indicates the base velocity, which is set to a non-zero value when considering the asymmetry of ebb and flow of tides. The values of parameters A and B determine the patterns of flow signal. When $|B/A| = 0$, the flow signal becomes a symmetrical tide signal. For $|B/A| \geq 1$, the signal represents a unidirectional flow with time-varying current velocity, normally used to simulate flow signals influenced by waves or the combined action of currents and waves. For asymmetrical tide signals, the theoretical value of $|B/A|$ should lie between 0 and 1. To investigate

Table 2
The optimal value of coefficients a, b and c in equation (35).

	U_s	U_{snd}	U_b	U_{bnd}
a	0.721	1.738	1.260	1.677
b	−0.623	−0.101	−0.054	0.087
c	0.498	0.502	0.496	0.501

the scour progression in both ebb and flow periods of tides, the maximum current velocity in the weaker half-cycles, equivalent to $|A| - |B|$, must exceed the threshold velocity for the initiation of scour around the pile. In this study, given a maximum current velocity of 0.25 m/s in the dominant flow direction, a reasonable range for $|B|$ is 0–0.04, and $|B| = 0.02$ is adopted for the asymmetrical tide scenarios. On the other hand, h indicates the water depth at a given time moment, and the parameter C represents the oscillation amplitude of the water depth. The variable D refers to the base water depth, which represents the normal water depth in the absence of tides.

To facilitate understanding, the flow velocity and water depth in the scenario of 'SqT60', 'SSinT60' and 'ASinT60' are plotted in Fig. 5 as an illustrative example.

It is worth noting that simulating the scour process demands significant resources, both in terms of computation time and computational capacity. As a result, the numerical model developed in this study is scaled down compared to real-world dimensions due to computational constraints. Leveraging this reduced scale, the computation time for each model has been reduced to approximately 140 h on a high-performance computer with 64 CPU cores and 64 GB RAM. This approach ensures practical feasibility without compromising calculation accuracy.

For efficiency, only the tide period equal to 60 min is scaled from a typical semidiurnal tide period in the real world, while other periods considered in this study are relatively shorter. Such an approach was designed in the study based on the following three reasons.

(1) Tide in the real world exhibits variability in period, underscoring the significance of exploring the impact of their period on scour progression.

(2) Besides regular tidal fluctuations, factors such as waves, tsunamis, and confluence flow near estuaries can also introduce irregular oscillations with periods spanning from seconds to hours.

(3) The approach enables us to obtain a diverse set of scour results across different tide periods within a reasonable computation time. This will facilitate the exploration of how tide periods influence scour progression.

In essence, despite the employment of scaled models, the outcomes of these calculations serve to enhance our understanding of scour progression amidst tidal dynamics, particularly in pinpointing the primary factors that govern scour progression.

3. Maximum scour depth development process

3.1. Influence of tide pattern on maximum scour depth development process

As mentioned earlier, some previous studies found that scour pits formed faster in periodic tides than in unidirectional tidal currents, while others found that scour pits formed more slowly in periodic tides than in unidirectional tidal currents. In order to understand the reason for these conflicting findings, this Section investigates the 120-min scour progression in five different scenarios with the same tide period but varying tide patterns. The five scenarios are 'Uni', 'SqT5', 'SSinT5', 'ASinT5', and 'ASinT5R', respectively. The calculated trend of the maximum scour depth over time in these five scenarios is shown in Fig. 6.

From Fig. 6, it is interestingly found that as the scouring time increases, the maximum scour depth in the 'Uni' scenario shows a steady

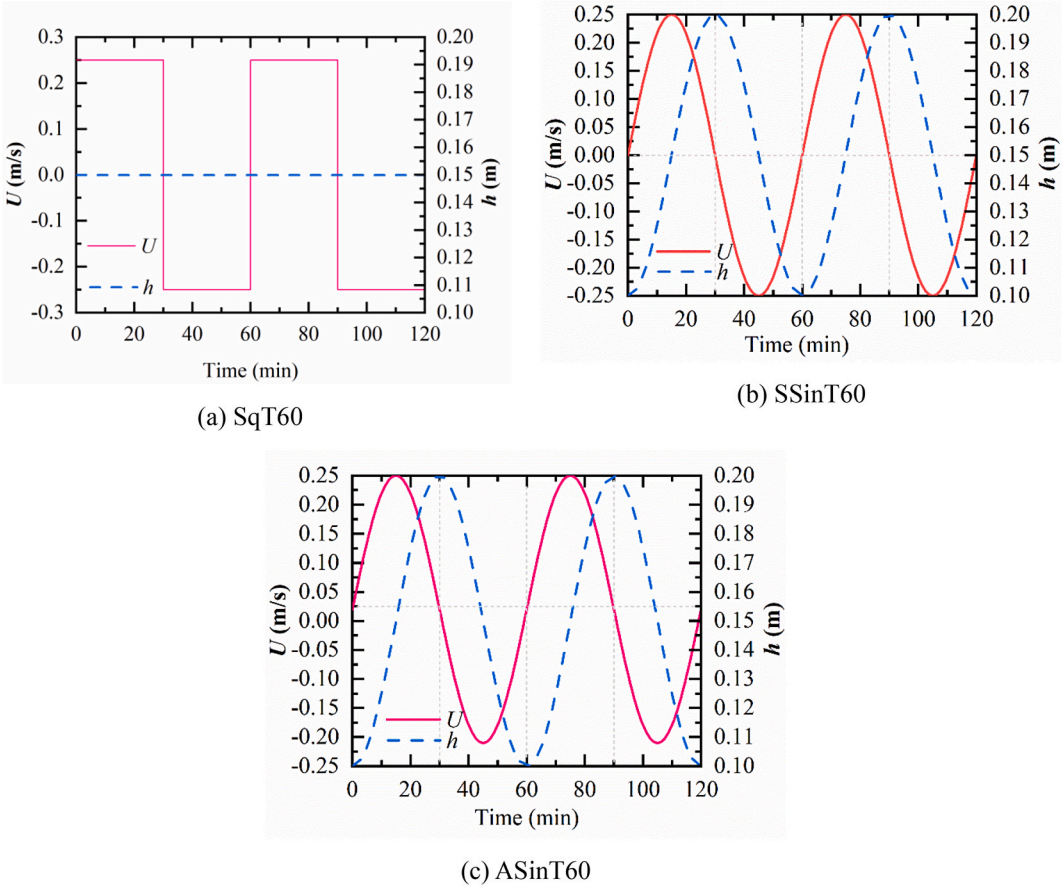

Fig. 5. Flow velocity and water depth signals during the ebb and flow of different types of tides: (a) SqT60; (b) SSinT60; (c) AsinT60.

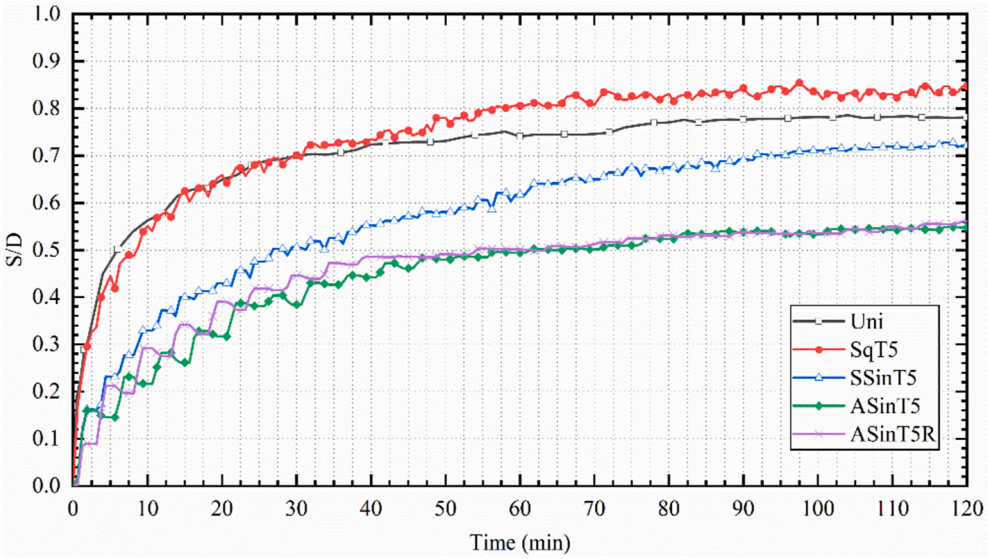

Fig. 6. Trend of the maximum scour depth over time in the scenarios with different tide patterns.

increase, whereas the maximum scour depth in the four periodic tide scenarios fluctuates in the process of growth, particularly during the early stage of scouring. The main reason for this can be attributed to the backfilling effect of repetitive reverse flow. To be specific, while the seabed is undergoing erosion, sediment transportation can take place in two ways. The first way is called advection, which refers to those sediment particles that are stirred up by vortices are carried away by the flow of water. The second way is referred to as bed load transport, where sediment particles are rolled or bounced along the seabed. When the direction of tidal flow shifts, the flow direction upstream and downstream of the monopile will reverse simultaneously. As a result, the upstream side that was present during the first half-cycle will become the downstream side, while the downstream side during the first half-cycle will transform into the upstream side. During this process, some sediment particles either suspended in the water or rolled on the seabed, which are moving downstream, may be brought back to their original positions by the reverse flow, resulting in a phenomenon known as backfilling. It is the repetitive backfilling by reverse flow that causes the fluctuation in the growth of the maximum scour depth in periodic tide scenarios. When the scour depth is shallow, a greater number of sediment particles near the monopile can be agitated by vortices or transported along the seabed by the water flow, resulting in more sediment particles being involved in the backfilling process. This leads to a more noticeable fluctuation in the growth of the maximum scour depth at the initial stages of scouring. As the scouring continues and the scour depth becomes deeper, fewer sediment particles are involved in the backfilling process, resulting in a gradual weakening of the fluctuation in the growth of the maximum scour depth.

From Fig. 6, it is also noticed that the fluctuation in the growth of the maximum scour depth is more pronounced in the 'ASinT5' and 'ASinT5R' scenarios when compared to the maximum scour depth in the 'SqT5' and 'SSinT5' scenarios. This is due to the fact that in the case of asymmetrical tide scenarios, either ebb or flow dominates the periodic tides, resulting in varying impacts of the tide's ebb and flow on scouring and backfilling. By contrast, in symmetrical tide scenarios, the tide's ebb and flow play an equivalent role in scour and backfilling, leading to smaller fluctuations in the growth of the maximum scour depth as shown in Fig. 6. In addition, Fig.6also shows that the maximum scour depth in the symmetrical tide scenarios develops faster than in the asymmetrical tide scenarios. The reason for this is also attributed to the distinctly different impacts of the tide's ebb and flow on scouring, which will be further discussed in Section 6.

Finally, Fig. 6 illustrates that the maximum scour depth in the 'Uni' scenario shows the fastest development within the first 30 min. The delay of the maximum scour depth in the periodic tide scenarios during this period can be attributed to the backfilling caused by the reverse flow. However, beyond the initial 30 min, the maximum scour depth in the 'SqT5' scenario surpasses that of the 'Uni' scenario and continues to deepen until the simulation calculation ends. This may be due to the fact that the scour pit in the 'Uni' scenario almost reaches an equilibrium state within the first 30 min, while the periodic scouring and backfilling in the 'SqT5' scenario lead to a different scour pit response angle and erosion area, which enable the continued growth of the scour pit around the monopile. The reason why a similar growth trend of the maximum scour depth is not observed in the 'SSinT5', 'ASinT5', and 'ASinT5R' scenarios is also related to the flow intensity that can cause 'effective scouring'. A further discussion about flow intensity and 'effective scouring' will be given in Section 6.

In summary, the results presented in Fig. 6 suggest that the tide pattern has a significant impact on scour progression, and even a shift in the dominant flow direction (such as in the 'ASinT5' and 'ASinT5R' scenarios) can cause variations in the scour progression. The 'square tide' scenarios exhibit a deeper scour pit, while the 'sinusoidal tide' scenarios exhibit a shallower scour pit, which is consistent with the previous findings (Schendel et al., 2019; Wang et al., 2024). Furthermore, the asymmetrical sinusoidal tide lead to the shallowest scour depth and slowest scour rate compared to unidirectional current and symmetrical tide.

3.2. Influence of tide period on maximum scour depth development process

Understanding the formation process of scour pits under different tide periods is of great significance to guiding the maintenance of OWT monopiles, as it can help better understand the mechanisms behind the formation of scour pits and then develop appropriate measures at right time to prevent the scour-induced damage to the monopiles. In view of this, the influence of the tide period in different tide patterns on scour progression will be investigated in the following.

First of all, the development trends of the maximum scour depth in the symmetrical scenarios with varying tide periods are calculated. The results are shown in Fig. 7.

From Fig. 7, it is found that the tide pattern does have a significant impact on the initiation and progression of scour pit. To be specific, regardless of the tide period, symmetrical square tides (referred to as 'SqT5' and 'SqT60') consistently result in a deeper scour pit near the

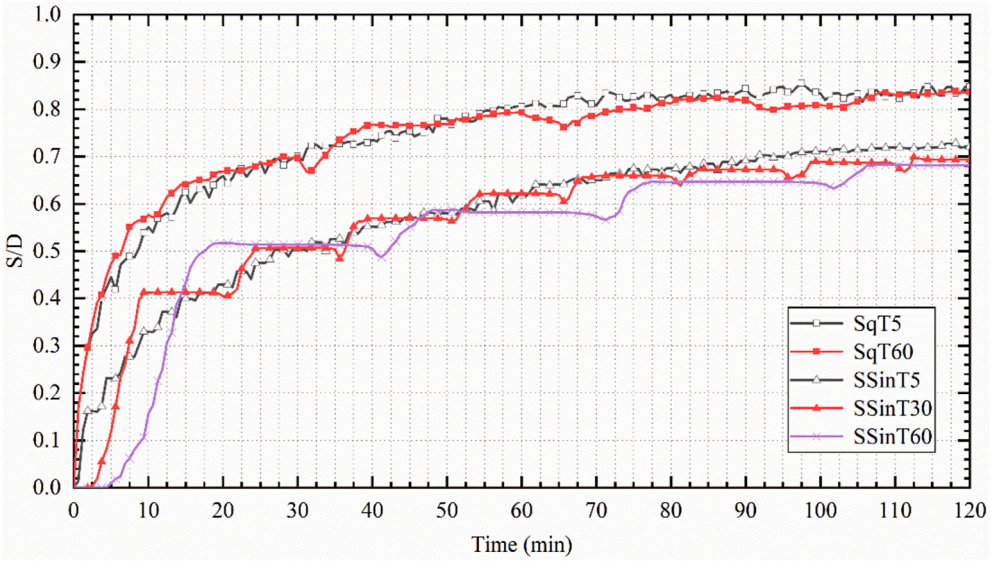

Fig. 7. Trends of the maximum scour depth in symmetrical tide scenarios with varying tide periods and patterns.

monopile compared to symmetrical sinusoidal tides (referred to as 'SSinT5' and 'SSinT60'). The rationale behind this is that the flow velocity in the symmetrical square tide scenarios remains at its maximum over time, leading to strong scouring to the seabed around the monopile, whereas the flow velocity in the symmetrical sinusoidal tide scenarios varies over time and it reaches and stays at its maximum only for a short period, which results in less severe scouring.

However, the natural rise and fall of tides exhibit an uneven variation in both flow velocity and water depth, which makes it necessary to investigate how the period of asymmetrical tides affects the formation and progression of scour pits. To explore this, the growing trends of the maximum scour depth in four asymmetrical tide scenarios with different tide periods, namely 'ASinT5', 'ASinT15', 'ASinT30', and 'ASinT60', are calculated. The calculation results are shown in Fig. 8.

From Fig. 8, two phenomena can be observed. The first phenomenon is that the shorter the period of the asymmetrical tide, the earlier the initiation of the scour pit will occur. For example, in the 'ASinT5' scenario, a distinct scour pit is visible at a scouring time of 2.5 min, whereas in the 'ASinT60' scenario, a scour pit is not clearly visible until a scouring time of 5 min. The second phenomenon is that the longer the period of the asymmetrical tide, the earlier the equilibrium scour depth of the scour pit can be reached. For example, in the scenario referred to as 'ASinT60', it takes 20 min for the scour pit to reach 90% of its equilibrium scour depth, whereas, in the 'ASinT5' scenario, it takes 80 min for the scour pit to reach the same scour depth. Such a phenomenon is slightly different from that observed in Fig. 7, which shows that the initiation of a scour pit occurs earlier when the period of the symmetrical tide is shorter, and a deeper scour pit is not always observed when the period of the symmetrical tide is longer.

Figs. 7 and 8 show that the scour depth development curves of both symmetrical and asymmetrical sinusoidal tides with longer periods remarkably exhibit periodic plateau stages, in addition to the increasing and decreasing stages. Similar findings have been observed by (Wang et al., 2024), who attributed this phenomenon to the periods with low current velocity that are insufficient to initiate sediment motion. As illustrated in Figs. 7 and 8, a longer period of sinusoidal tide can typically lead to longer plateau stages in each cycle.

An interesting phenomenon is that the variation of tide period can

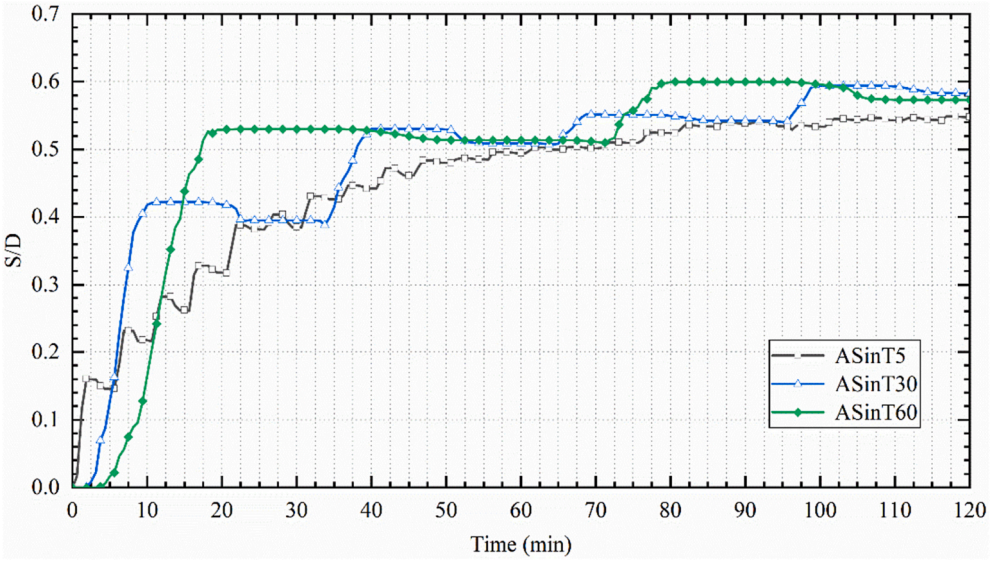

Fig. 8. Trends of the maximum scour depth in asymmetrical tide scenarios with varying tide periods.

only affect the scour process in each cycle and the general scour progression, it has little effect on the equilibrium scour depth, provided that the scour time is sufficiently long. This is attributed to the similar normalized cumulative effective flow intensities of scenarios with same tide pattern, even with various tide periods. The concept of normalized cumulative effective flow intensity and its effect on equilibrium scour depth will be further discussed in section 6. When considering same number of tide cycles, it is observable that tides with longer periods generally lead to deeper scour depths compared to those with shorter periods, consistent with the observation proposed by Whitehouse and Stroescu (2023). This phenomenon arises from the fact that a longer period allows for a longer scouring time within a consistent number of cycles, thereby resulting in a deeper scour depth.

4. Comparison of scour depth development process at fore and back sides of the pile

4.1. Influence of tide pattern on the asymmetry of scour progression at fore and back sides of the pile

The comparison of scour depth development progressions at the fore and back sides of the pile under various tide patterns as well as corresponding unidirectional current is illustrated in Fig. 9. Fig. 9 (a) presents a comparison of scour development at fore and back sides (180° versus 0°), while Fig. 9 (b) depicts the comparison at the laterally-fore and laterally-back sides (135° versus 45°). Scour depths in all scenarios are normalized by the pile diameter D. Given that the fore and back sides of the pile vary periodically with the reversals of flow direction of tides, they are defined relative to the flow direction in the initial stage of the scour process to facilitate depiction and understanding. For clarity, the relative position of the four specific data monitoring points (180° versus 0°, 135° versus 45°) around the pile, along with the flow direction at the initial stage of the scour simulation, are shown in Fig. 9.

The hollow dots plotted along the curves in Fig. 9 represent data points at the end of each half cycle of the tide scenarios. Additionally, diagonal lines are plotted in Fig. 9 as reference lines, with data points along these lines indicating equivalent scour depths at the fore and back sides of the pile.

As shown in Fig. 9(a), the scour depth development progression of the unidirectional current scenario exhibits an increase in front of the pile ($S_{180^\circ}(t)/D$) during the initial stage, accompanied by a decrease at the back side ($S_{0^\circ}(t)/D$). The decrease implies the deposition at the back side of pile caused by lee wake turbulent in the initial stage. Following the initial stage, a turning point in the pairwise scour data of the unidirectional current scenario emerges, followed by a prolonged period of steady process. Herein the 'steady process' refers to a consistent ratio of scour depth development speeds at the fore and back sides of the pile, rather than a steady scour rate in the time domain. The curve during this steady process is approximately parallel to the diagonal lines ($S_{180^\circ}(t) : S_{0^\circ}(t) = 1{:}1$), indicating an equivalent scour rate at the fore and back sides of the pile after the initial stage. A similar development pattern can also be discovered from the comparison of scour progressions at the laterally-fore and laterally-back sides of the pile (see 'Uni' in Fig. 9(b)). The primary difference is that the decrease in scour depth at laterally-back side is relatively lower than that at the back side, suggesting that deposition mainly occurs at the backed side. Despite this difference, a turning point still exists in the trajectory of the comparison between the laterally-fore and laterally-back sides.

More turning points can be discovered in the trajectory of periodic tide scenarios. Taking the trajectory of the square tide scenario in Fig. 9 (a) as an example, the scour depth at the fore side of the pile initially increases, accompanied by a deposition process at the back side simultaneously. Then, a turning point emerges at the end of the first half cycle, followed by a dramatic increase in scour depth at the back side and a slight decrease at the fore side of the pile until the flow direction reversing again. This alternating process repeats with the increase of tide cycles until the scour progression reaches a relatively equilibrium stage, consistent with previous findings (Whitehouse and Stroescu, 2023; Wang et al., 2024). As can be accounted from Fig. 9, the number of hollow dots in each scenario is fewer than the total number of half cycles ($N = t/(0.5T) = 48$). This is because the symbols for cycles after the equilibrium stage are neglected. Therefore, the top right short tail after the last hollow dot on the trajectory of each tide scenario refers to the scour depth development process in the equilibrium stage. Despite the number of tide cycles, only slight scour occurs in this stage. In the view of the whole scour progression, the fluctuation of scour depth development at the fore and back sides of the pile decreases with the tide cycles.

Fig. 9(a)–(b) show that the scour depth development trajectories of all tide scenarios always turn at the hollow dot point, indicating the scouring and backfilling processes at the fore ($S_{180^\circ}(t)$ and $S_{135}(t)$) and back ($S_{0^\circ}(t)$ and $S_{45^\circ}(t)$) sides always alternate at the end of each half cycle. However, it's important to note that the scour and backfilling processes do not necessarily start and terminate precisely at the beginning and end of each half cycle when the flow direction reverses. To further illustrate it, the time development of normalized scour rates at four specific positions around the pile ($0^\circ, 45^\circ, 135^\circ, 180^\circ$) in all tide scenarios with a period of 60 min are plotted in Fig. 10 along with the tide cycles. The normalized scour rate, defined as the gradient of the normalized scour depth time development curve, indicates the increase or decrease rate of scour depth at each specific time point.

Fig. 10(a) shows that the scour rate in front of the pile ($135^\circ, 180^\circ$) increases at the start of the first half cycle, reaching a local maximum value immediately, followed by a gradual decrease during this half

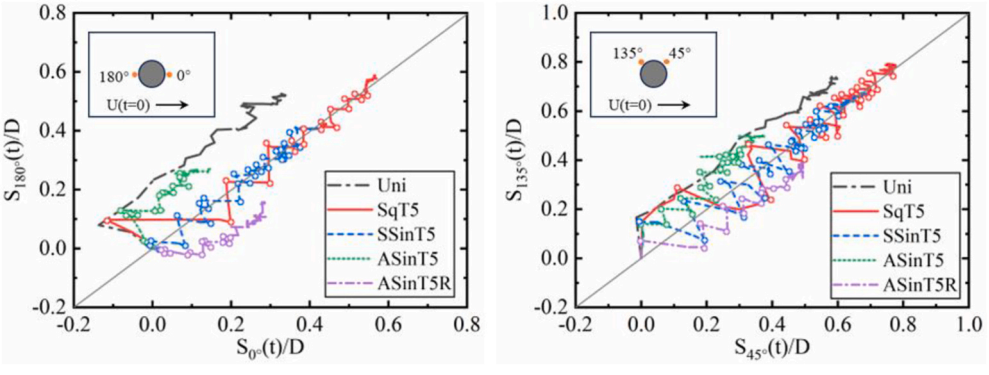

(a) (b)

Fig. 9. Comparisons of scour depth development process on: (a) fore (180°) and back (0°) sides of the pile; (b) lateral-fore (135°) and lateral-back (45°) sides of the pile. The hollow dots refer to data points at the end of each half tide cycles.

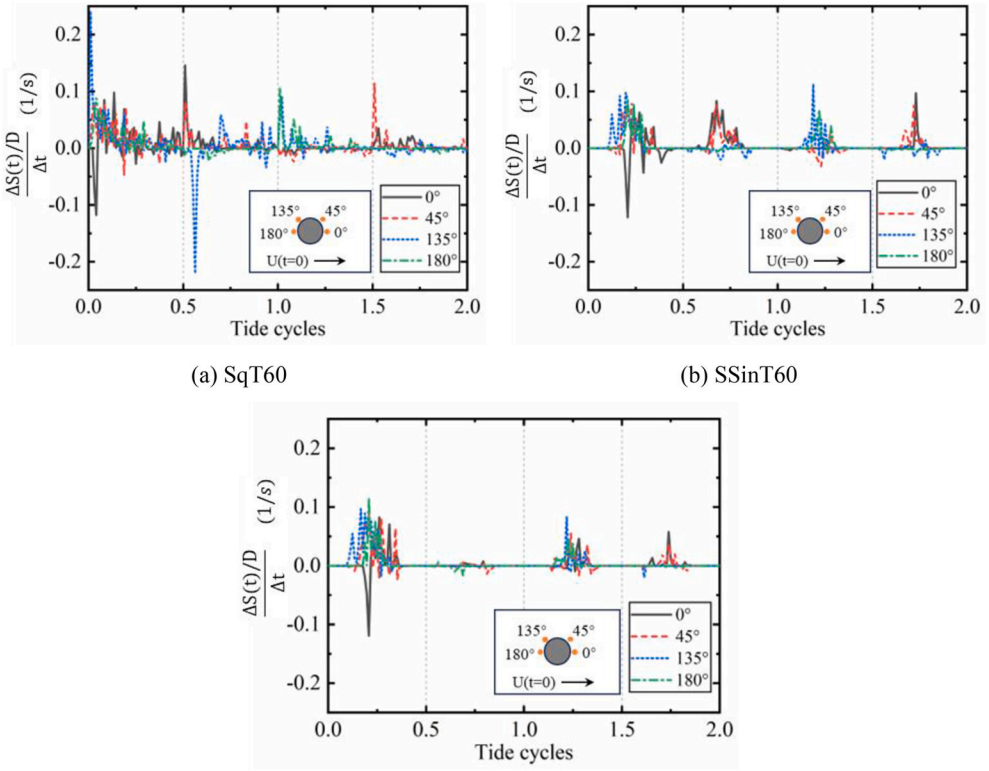

Fig. 10. Scour depth development rates at fore (180° and 135°) and back (0° and 45°) sides of the pile under various tide patterns: (a) Square tide (T = 60 min); (b) Symmetrical sinusoidal tide (T = 60 min); (c) Asymmetrical sinusoidal tide (T = 60min).

cycle. At the end of the first half cycle (i.e., the start of the second half cycle), the scour rate in front of the pile (135°,180°) turns negative and reaches a local minimum value immediately, while the scour rate at the back side (0°, 45°) rises to a local maximum value and then gradually decrease. Despite the decrease in scour rate (or backfilling rate indicated by the negative value of scour rate) in each half cycle, the value does not reach and remain at 0 for a considerable time duration until the final cycle when the scour pit reaches an equilibrium stage. This indicates that, for the square tide scenario, the scouring and backfilling processes run through the entirety of each half cycle before equilibrium stage, although the rates may gradually decrease. In contrast, sinusoidal tide scenarios (shown in Fig. 10(b-c)) exhibit a significant difference from the square tide with regards to the development of scour rate in each half cycle. Fig. 10(b-c) shows that the scour rates at all four positions remain at 0 for a remarkable time duration both before and after the start or end of each half cycle, implying a shorter scouring and backfilling process in each half cycle compared to the square tide. Besides, the increase in scour rates in sinusoidal tide scenarios is slower than in square tide scenarios, and the local maximum value is also much lower. This is consistent with previous findings (Schendel et al., 2018, 2019; Wang et al., 2024), and can be attribute to the effective flow velocity. It is well understood that the scouring or backfilling process will not occur when the magnitude of current velocity is lower than a critical value. For a sinusoidal tide pattern illustrated in Fig. 5, the current velocity varies continuously with time in each half cycle. As a result, the magnitude of the current velocity near the start or end of each half cycle is much lower than the critical value for scouring or backfilling, corresponding to the zero scour rate periods in Fig. 10(b-c). For the asymmetrical tide scenario shown in Fig. 10(c), the scour or backfilling rates in the second half cycle are much lower than in the adjacent previous or next half cycle, but this phenomenon is not noticeable in the corresponding symmetrical tide scenario shown in Fig. 10(b). This can be attributed to the asymmetry of peak current velocities in the ebb and flow cycles of asymmetrical tide scenarios, in which the higher current velocity in the dominant cycles can always result in a higher scour rate than in the adjacent reversed current cycles.

Due to the variation in tide patterns, the scour depth development trajectories at the fore and back sides of the pile of tide scenarios shown in Fig. 9 exhibit great differences. Firstly, the fluctuation of the 'Sq' scenario is larger than that of the 'SSin' scenario, while the fluctuation of the 'ASin' scenario is the smallest consistent with the trends observed in equilibrium scour depths (Fig. 6) and scour rates (Fig. 10) of various scour patterns. Another notable difference is the asymmetry of the scour development process at the fore and back sides of the pile. The development trajectories of symmetrical tide scenarios, including 'Sq' and 'SSin' scenarios, develop along the 1:1 line and cross it in each half cycle, indicating a symmetrical scour process at the fore and back sides of the pile, as will be further illustrated in the three-dimensional scour hole profile in the next section. In contrast, the development trajectories of 'AsinT5' scenario mainly distribute to the left of the 1:1 line, similar to the 'Uni' scenario, indicating that the deeper scour depth in front of the pile through the whole scouring process. This asymmetry, to be further illustrated in section 5, arises from the asymmetry of ebb and flow of tides. Specifically, higher current velocity during the flow cycle leads to deeper scour in front of the pile and more deposition at the back side compared to the subsequent ebb half cycle with relatively lower current velocity. Conversely, trajectories of the 'AsinT5R' scenario mainly distribute to the right of the 1:1 line, suggesting deeper scour at the back side than the fore side. This difference can be attributed to the opposite predominant current directions in scenarios 'AsinT5' and 'AsinT5R'.

4.2. Influence of tide period on the asymmetry of scour progression at fore and back sides of the pile

Fig. 11 depicts the variation of scour depth development trajectories with different tide periods. It shows that the development trajectories of

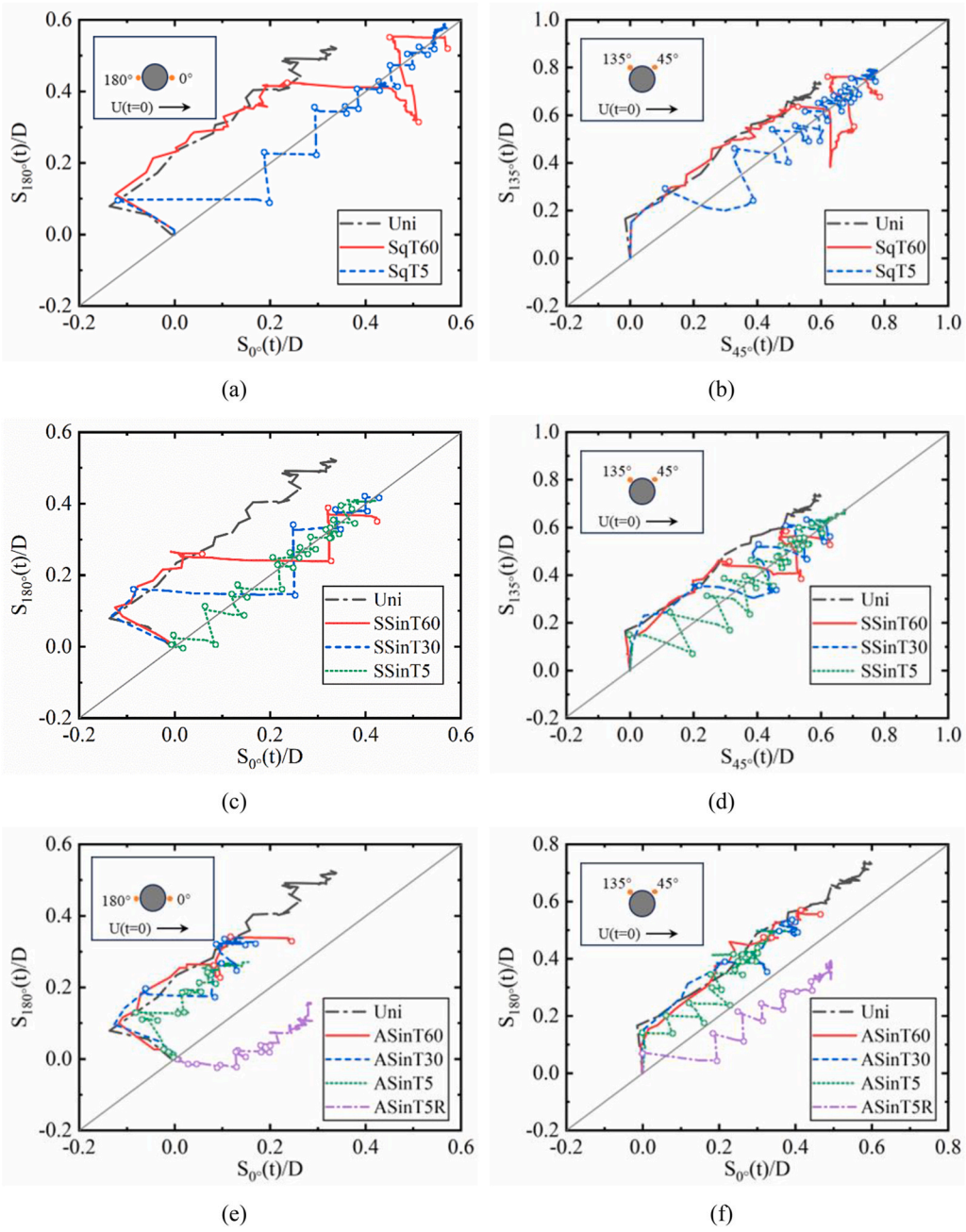

Fig. 11. Comparisons of scour depth development progressions at fore (180° and 135°) and back (0° and 45°) sides of the pile under various tide patterns and periods: (a)–(b) Square tides; (c)–(d) Symmetrical sinusoidal tides; (e)–(f) Asymmetrical sinusoidal tides.

tides with longer period exhibit larger amplitudes and wider spans along the development direction in each half cycle, compared to those with same tide pattern but shorter tide period. The asymmetries in scour depth development processes at 180° versus 0° and 135° versus 45° are significantly affected by the tide periods, especially in the early cycles before the equilibrium stage. But this effect gradually decreases with the increase of tide cycles as well as the development of maximum scour depth, until the equilibrium stage when scour depths at all positions show no noticeable development. The effect of tide period on the asymmetry of scour progression is more pronounced in symmetrical tide scenarios (Fig. 11(a-d)) than in asymmetrical tide scenarios (Fig. 11(e-f)). Therefore, despite the generally symmetrical scour pits at the end stage of symmetrical tide scenarios, a remarkable asymmetry of scour depths at the fore and back sides can be observed during the development process. This asymmetry in scour progression increases with the tide period and has a maximum limit equivalent to that produced by the corresponding unidirectional current with a constant current velocity equivalent to the peak current velocity of the tide.

5. Three-dimensional scour hole profile

In the last section, four representative positions around the pile were selected to investigate the asymmetry of scour depth during the scour development progression, through comparisons of scour depths and scour rates over time. It is meaningful and helps improve understanding of the temporal development of scour pit asymmetry. However, it has limitations in depicting the overall shape and asymmetry of the scour pit. To address this limitation, three-dimensional scour holes are produced in this section. The output data from Flow3D-HYDRO is imported into EnSight software, which is then used to create the three-

dimensional (3D) morphologies of scour pits for detailed analysis. The following section provides an in-depth depiction of the research findings.

As shown in Fig. 12, the scour pits formed in unidirectional tidal currents usually takes on a spoon-shaped morphology in ideal experimental conditions where the sediment and inlet flow are homogeneous. Specifically, the scour pit is typically characterised by left-right symmetry and front-back asymmetry. The deepest depth of the scour pit tends to occur at the lateral-fore side of the monopile, while the back side of the scour pit is relatively shallow and extends further, often ending with a sediment hump. These findings have been widely reported in previous studies.

However, the 3D morphology of the scour pit can vary due to multiple factors that affect its formation. One of these factors is the tide period and tide pattern, which influences the velocity, direction, and duration of the water flow, thereby giving rise to diverse 3D morphologies of the scour pits. To investigate the influence of the tide period and pattern on the 3D morphology of the scour pit, Fig. 13 a-f show the 3D morphologies of the scour pits that are formed after 2 h of scouring in periodic tides with varying tide periods and patterns.

From Fig. 13, the following phenomena can be observed.

- *Phenomenon* 1 – Despite the difference in tide period and tide pattern, the 3D morphologies of the scour pits, especially those formed in symmetrical tide scenarios, exhibit both left-right and front-back symmetry, which is distinctly different from those spoon-shaped scour pits formed in unidirectional tidal currents. The front-back symmetry observed in these scenarios is believed to be a result of the periodic shift of the flow direction during the tide's ebb and flow. In contrast to the symmetrical tides, asymmetrical tides typically result in front-back asymmetry of scour pit. These phenomena are consistent with the findings in previous section.
- *Phenomenon* 2 – Compared to the corresponding longer period symmetrical tides (e.g., 'SqT60' and 'SsinT60'), the shorter period symmetrical tides (e.g., 'SqT5' and 'SSinT5') lead to a larger erosion area and a larger scour pit around the monopile.
- *Phenomenon* 3 – Irrespective of the tide period, symmetrical square tides (e.g., 'SqT60' and 'SqT5') can always create a larger erosion area and a larger scour pit around the monopile than symmetrical sinusoidal tides (e.g., 'SSinT60' and 'SSinT5') do.
- *Phenomenon* 4 – Compared to the erosion area and scour pit formed in symmetrical sinusoidal tides (e.g., 'SSinT60' and 'SSinT5'), the erosion area and scour pit formed in asymmetrical sinusoidal tides (e.g., 'ASinT60' and 'ASinT5') are much smaller.

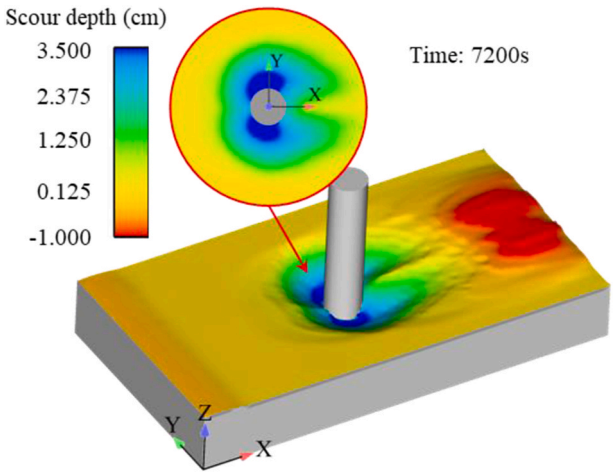

Fig. 12. The 3D morphology of the scour pit generated in unidirectional tidal currents.

In order to understand the above phenomena 2–4 observed from Fig. 13, the flow velocities around the monopile and the shear stresses on the seabed in each periodic tide scenario at the moment when the flow reaches its maximum velocity are illustrated in Fig. 14. Since 'ASinT60' and 'ASinT5' consider the asymmetry of tides, to ease understanding, Fig. 14(e) and f demonstrate the flow velocities and shear stresses at the moment when the flow reaches its maximum velocity in the first half cycle of the tides, and Fig. 8g and h shows the flow velocities and shear stresses at the moment when the flow reaches its maximum velocity in the second half cycle of the tides. In addition, it should be highlighted that each subplot in Fig. 14 features two legends, one is for illustrating the velocity of the flow surrounding the monopile, and the other for depicting the shear stress exerted on the seabed surface around the monopile.

From Fig. 14, it is found that phenomenon 2 observed in Fig. 13 can also be confirmed by comparing Fig. 8a and c with Fig. 8b and d. The latter shows larger scour pits and erosion areas than the former due to two reasons. Firstly, in the 'SqT5' and 'SSinT5' scenarios, high shear stress exerts on a larger downstream area compared to those in the 'SqT60' and 'SSinT60' scenarios. This results in sediment particles in a larger downstream area being taken away by water flow from their original positions. Secondly, the long period of flow in the 'SqT60' and 'SSinT60' scenarios creates a bigger sediment hump on the downstream side of the monopile. When the direction of water flow reverses, this sediment hump will be flushed by the reverse flow and more sediment particles will be brought back into the scour pit, exhibiting a more evident backfilling phenomenon. This can be observed from Fig. 14(a) and c where the yellow colour areas in the upstream direction of the monopile have reached to the edge of the scour pits, while the yellow colour areas in the upstream direction of the monopile in Fig. 14(b) and d are far to the edge of the scour pits.

The reason for Phenomenon 3 observed in Fig. 13 can be explained by the larger erosion areas highlighted in red and yellow colours on both sides of the monopile in Fig. 14(a) and b, as opposed to Fig. 14(c) and d. A larger erosion area denoted by red and yellow colours signifies that a larger region of the seabed surface experiences high shear stress. The Phenomenon 4 observed in Fig. 13, i.e., the smaller erosion area and scour pit formed in asymmetrical sinusoidal tides (e.g., 'ASinT60' and 'ASinT5'), can be easily understood by observing Fig. 14(e-h). From Fig. 14(e-h), it is seen that in these asymmetrical tide scenarios, only the flow in the dominant direction causes significant seabed erosion, whereas the erosion by the reverse flow is much weaker.

6. Prediction method for scour depth development process in periodic tides

6.1. Characteristic current velocity method and effective flow work method

The calculation results presented above suggest that the tide period and tide pattern have a notable impact on the development of scour pits and their ultimate equilibrium scour depth, regardless of whether the ebb and flow of the tides are symmetrical or not. Schendel et al. (2018) tried to account for this phenomenon and predict the scour depth based on 'flow intensity', which can be simply described using either 'the maximum peak velocity U_{max}' or 'RMS flow velocity U_{rms}' of the tides. In their study, as U_{max} was found resulting in an overestimation of both scour progression and equilibrium scour depth, U_{rms} was recommended to better characterise the scour progression in periodic tides. U_{rms} can be described using the following equation:

$$U_{rms} = \sqrt{\frac{1}{N}\sum\left(\int |U(t)|dt\right)^2} \tag{21}$$

where $U(t)$ refers to the instantaneous flow velocities over the period of half tidal cycles, and N is the total number of half tidal cycles.

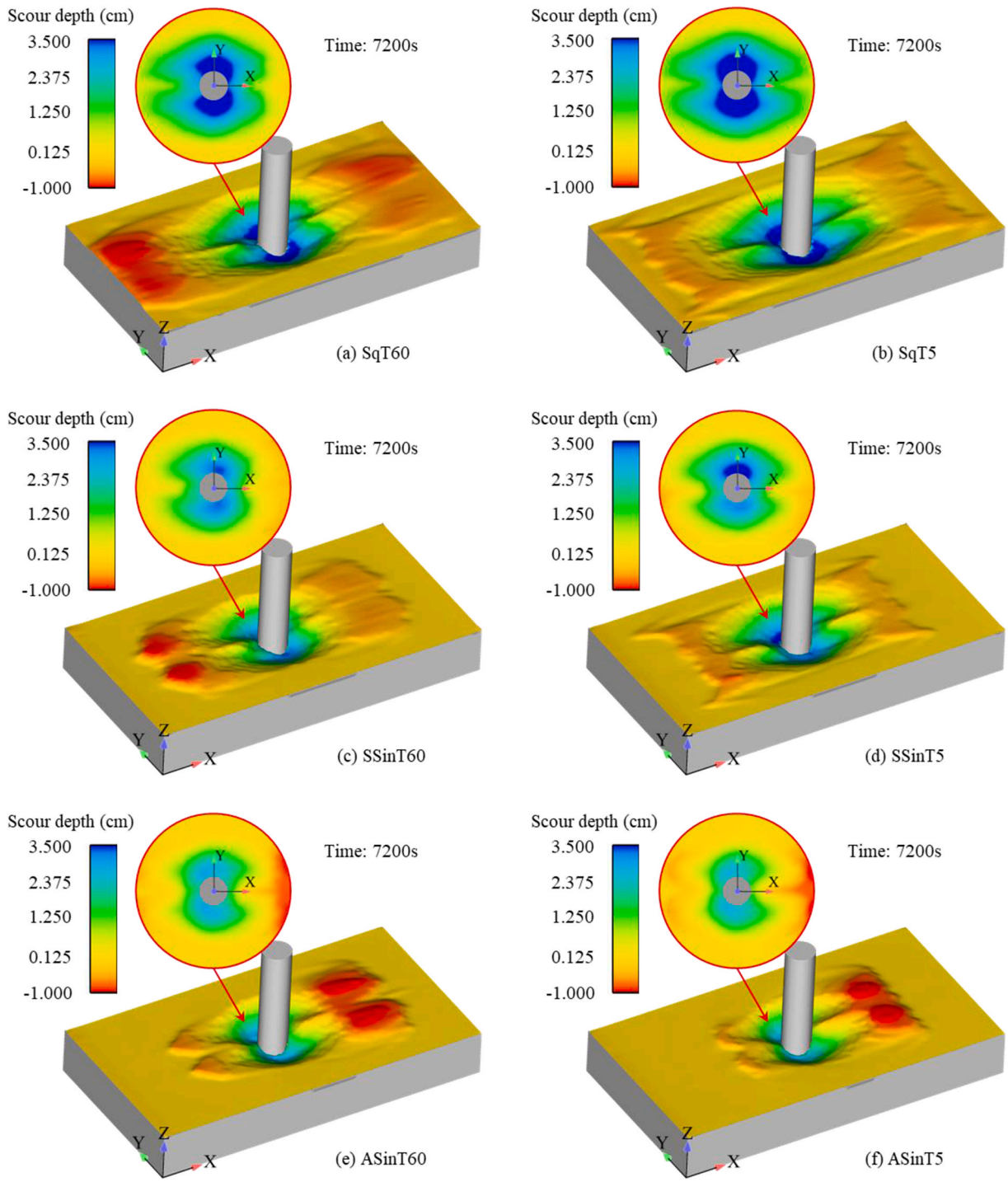

Fig. 13. The 3D morphologies of scour pits formed in periodic tides with varying tide periods and patterns.

However, the RMS flow velocity U_{rms} defined in (21) is not perfect in predicting the progression of scour depts due to the lack of consideration of critical flow velocity. It is well known that the movement of sediment particles on seabed surfaces depends on multiple factors such as sediment size, shape, density, water properties and so on. In other words, the occurrence of effective scouring will not happen until the critical shear stress, i.e., the minimum shear stress required to initiate sediment motion, is reached. The value of the critical shear stress varies from case to case, depending on the aforementioned factors in the local water area. This implies that in the ebb and flow of tides, not all tide flow can lead to effective scouring. Only those that can result in shear stress exceeding the critical shear stress can cause effective scouring. Based on this concept, Link et al. (2017) and Pizarro et al. (2017) proposed the concept of dimensionless effective flow work (DEFW) W^* to predict the scour depth in time-varying current profiles. In their research, the scour process was conceptualized as the work performed by near-bed currents in moving sediment particles. Thereby, the effective flow work represents the effective work imposed by near seabed current on the movement of seabed sediment particles around the pile. The dimensionless effective flow work is expressed as a function of effective flow velocity, as given by equation (22), where the effective current velocity was expressed in the form of the excess value of U above a critical current

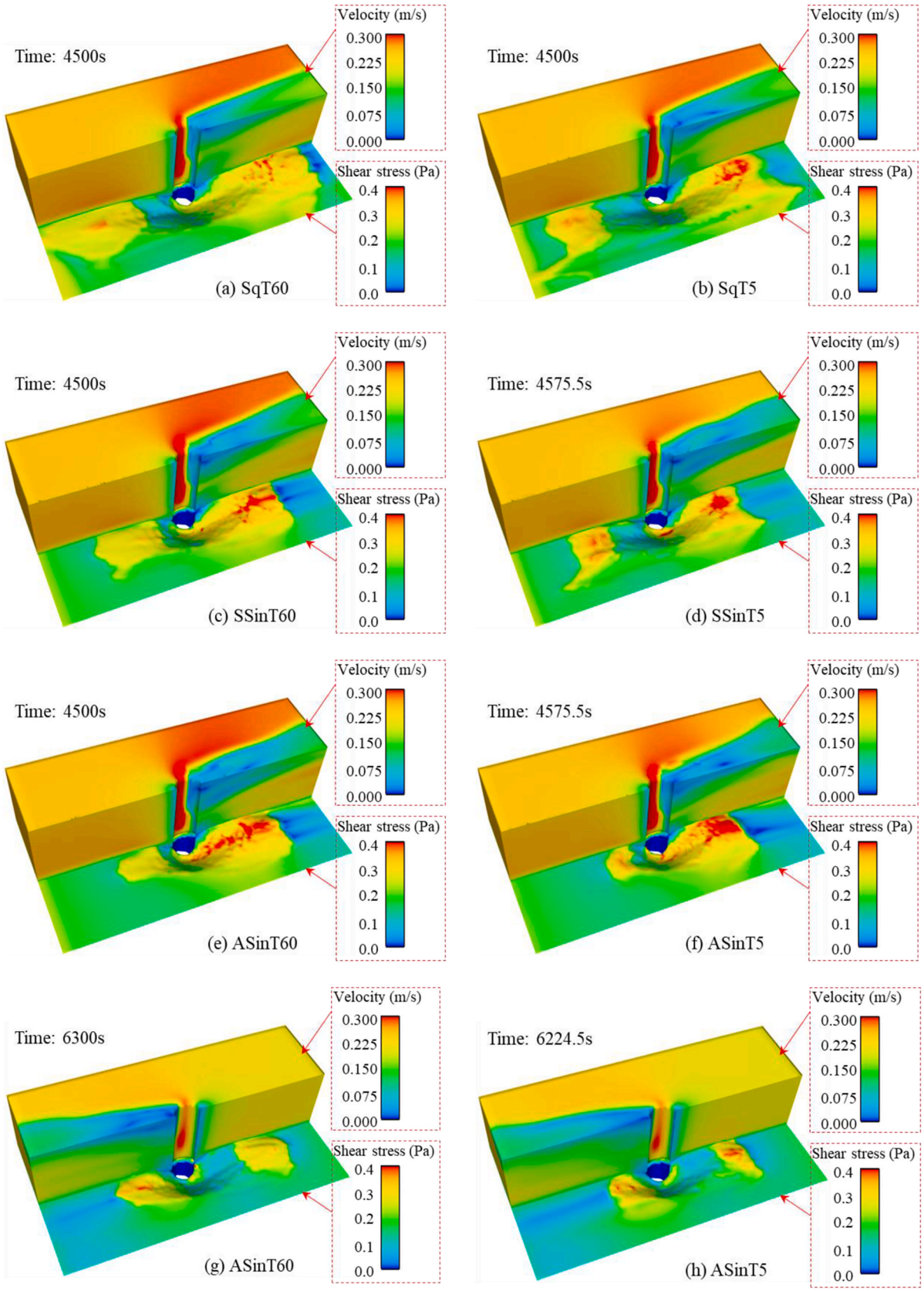

Fig. 14. Flow velocities around the monopile and shear stresses on the seabed surface near the monopile.

velocity U_{cr}.

$$W^* = \int_0^{t_{end}} \frac{1}{T_R}\left(\frac{U - \alpha U_{cr}}{U_R}\right)^4 \delta dt \tag{22}$$

where, t represents time; U is the current velocity may vary over time; U_{cr} denotes the critical current velocity required to initiate bed sediment particle motion in the far field form the pile; t_{end} indicates the time point at the end of the whole scour progression; U_R refers to the reference velocity and defined by:

$$U_R = \sqrt{(s-1)gd_{50}} \tag{23}$$

where s is the specific weight of the sediment particle, given by $s = \rho_s/\rho$, with ρ_s and ρ represent the densities of sediment particle and water, respectively; g is the acceleration of gravity; d_{50} refers to the median diameter of the sediment particles.

In addition, T_R in equation (22) denotes the reference time, defined as:

$$T_R = \frac{z_R}{U_R} \tag{24}$$

where z_R is the reference length and given by:

$$z_R = \frac{D^2}{2d_{50}} \tag{25}$$

Furthermore, the δ in equation (22) represents a Dirac–Delta function:

$$\delta = \begin{cases} 0, U < \alpha U_{cr} \\ 1, U \geq \alpha U_{cr} \end{cases} \tag{26}$$

where α is the reduction coefficient of the critical current velocity for the initialization of bed sediment particle motion, driven by the amplification effect of bed shear stress around the pile. Breusers et al. (1977) suggested a value of $\alpha = 0.5$. In other word, the bed sediment particles around the pile start moving when current velocity reaches or exceeds 0.5 U_{cr}.

Equation (26) means that only time periods with real-time current velocities equivalent to or exceed 0.5 U_{cr}, defined as the effective periods, will be considered in the calculation of the dimensionless effective flow work in equation (22). For illustration, the effective scouring periods of a symmetrical sinusoidal tide signal are illustrated in Fig. 15(a), considering two whole tide cycles as an example. The current velocity signal is plotted in the form of magnitude velocity, indicating that adjacent half cycles exhibit opposite flow directions.

Pizarro et al. (2017) presented that the equilibrium scour depth of a time-varying current velocity is highly correlated with its effective flow work. The mapping relations between them provide a possible means to predict the equilibrium scour depth. Based on this concept, Schendel et al. (2019) suggested that the equilibrium scour depth produced by a periodic tide can be calculated using the corresponding dimensionless effective flow work, as follows:

$$\frac{S_{eq}}{z_R} = c_1[1 - \exp(-c_2 W^{*c_3})] \tag{27}$$

where c_1, c_2 and c_3 represent the fitting coefficients, suggested to be 1.5250, −0.1170 and 0.2843 by Schendel et al. (2019) based on regression analysis of experimental data (Schendel et al., 2018, 2019).

Lately, more scour experiments considering various tide periods (Whitehouse and Stroescu, 2023) and peak velocities (Wang et al., 2024) have been conducted. Based on the experimental data, Wang et al. (2024) updated the optimal values of aforementioned coefficients and classified them into two sets for the scour depth prediction of unidirectional currents ($c_1 = 1.3982$; $c_2 = 0.1374$; $c_3 = 0.3000$) and periodic tides ($c_1 = 1.2834$; $c_2 = 0.0721$; $c_3 = 0.3641$), respectively.

Equation (27) provides a novel method to predict equilibrium scour depth in periodic tides, which has been demonstrated to exhibit a well-fitting performance within range of the aforementioned experimental data (Schendel et al., 2018, 2019; Whitehouse and Stroescu, 2023; Wang et al., 2024). This method, based on effective flow work, offers higher accuracy and a more reasonable and interpretable mechanism compared to previous approach utilizing U_{rms} or U_{max} to predict scour depths in unidirectional currents and extending them into the tidal scenarios. However, despite these advancements, certain limitations persist. Firstly, the effective flow work method was originally proposed for predicting scour depth in unsteady but unidirectional currents, characterized by a monotonous progression (Link et al., 2017). Consequently, it was assumed that the effective periods with current velocities exceeding 0.5 U_{cr} always have a positive effect on the scour process (Schendel et al., 2019). As illustrated in Fig. 15(a), the current velocity U during the effective period in each half cycle was involved in the calculation of W^* in the form of $(U - \alpha U_{cr})^4$ in equation (22), implying that the entire shaded area in each half cycle in Fig. 15(a) contributes positively to W^*, consequently enhancing equilibrium scour depth according to equation (27). However, the scour progressions of the tide scenarios, as shown in Figs. 6 and 11, are characterized by periodic scouring and backfilling processes, notably distinguished from the monotonous scour process observed in previous studies (Link et al., 2017; Pizarro et al., 2017). As a result, the effective periods in the second

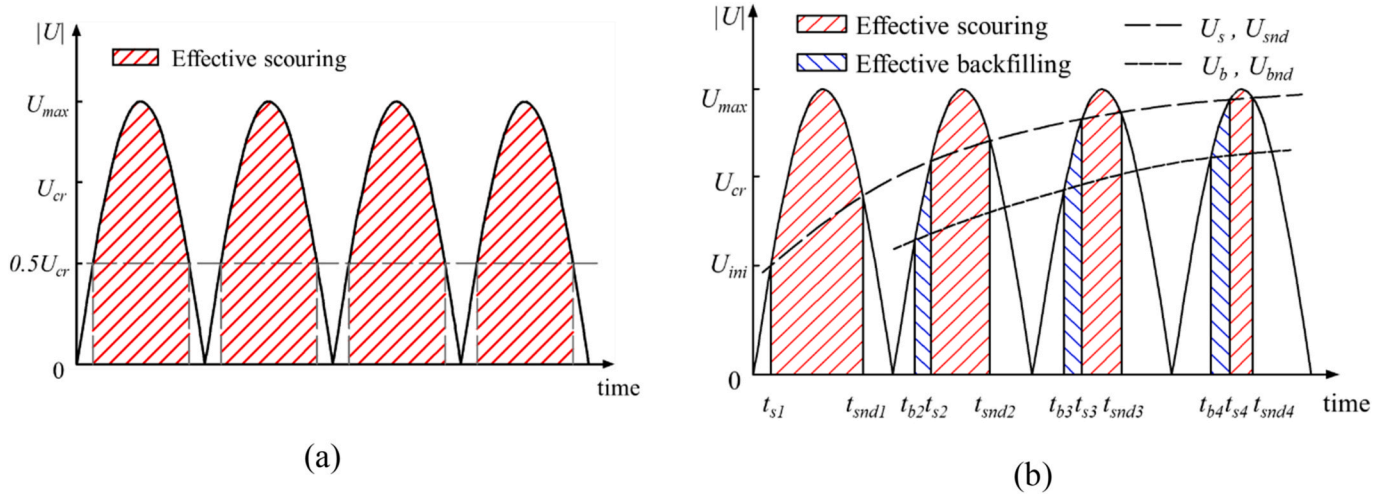

Fig. 15. Effective flow velocity diagram considering (a) constant and (b)time varying critical velocity respectively, for sediment particles motion.

and subsequent half cycles should be divided into two subperiods as illustrated in Fig. 15(b), with the previous subperiod in each half cycle responsible for backfilling process, while the latter correlates to the scouring process. In addition, the critical velocity for sediment particle motion around the pile, illustrated by the horizontal dashed line in Fig. 15(a), was hypothesized to be constant at 0.5 U_{cr} for simplification in the derivation and calculation of equation (22), whereas it should vary with tide cycles in practice. Furthermore, the critical velocities for backfilling and scouring around the pile should also differ, even within the same half cycles.

6.2. Development of critical velocities for scouring and backfilling

Wang et al. (2024) discovered that in sinusoidal tide scenarios, scouring occurs when the current velocity exceeds certain threshold, and ceases when it drops below another higher threshold. Both of these threshold velocities increase progressively as the number of tidal cycles increases. Drawing from this insight and the scour development progressions depicted in Fig. 5, the effective scouring and backfilling periods, corresponding to the scour depth increase and decrease processes shown in Fig. 5, are simplified and illustrated in Fig. 15(b). In Fig. 15(b), the development of critical velocities for scouring (U_s for initialization of scouring, U_{snd} for end of scouring) and backfilling (U_b for initialization of backfilling, U_{bnd} for end of backfilling) are considered separately. The t_s, t_{snd}, t_b and t_{bnd} are the characteristic time points for the initialization and end of scouring and backfilling processes in each half cycle, with numerical subscripts indicating the serial number of half cycles.

As illustrated in Fig. 15(b), the scouring process initiate at t_{s1} when the current velocity reaches a critical value U_{s1} for the initialization of sediment particle motion around the pile. It pauses at t_{snd1} when the current velocity drops to U_{snd1}, which is insufficient for sustaining a continuous scouring process due to the weakening effect of the existing scour pit on seabed shear stress. Following the reversal of flow direction, backfilling commences at t_{b2} when the current velocity reaches a critical value U_{b2} for backfilling in the second half cycle. The backfilling process ceases and converts to a scouring process as soon as the current velocity reaches U_{s2}, the critical velocity for scour in the second half cycles, at the time point t_{s2}. It then pauses after t_{snd2} when current velocity decreases below U_{snd2}. This scouring-backfilling process repeats with tide cycles until the equilibrium stage when neither scouring nor backfilling is noticeable.

With the development of scour pit, the kinetic energy of water flow is dissipated within the scour pit around the pile. As a result, a higher section-average current velocity is required to induce further scouring. This rule is illustrated in Fig. 15(b), where the critical velocities for initializing and ending of scouring process (U_s and U_{snd} respectively) increase with tidal cycles. Similarly, the critical velocities for the backfilling processes (U_b and U_{bnd}) follow a comparable increasing pattern. It is worthy to clarify that the critical velocities referenced here are generalized concepts. They represent the velocities at the specific time points when the scouring or backfilling process initialized or ended in each half-cycle. This differs from the well-known specific concept of critical velocity U_{cr} which refers to the threshold velocity needed to the initiate sediment motion on a flat seabed with absence of the pile. U_{cr}, combined with the pile diameter D, determines the critical velocity U_{ini} for the initiation of sediment particle motion around a pile. As illustrated in Fig. 15(b), the U_{ini} is a specific value of U_s in the first half-cycle. Considering all the impact factors on the development of critical velocities for scouring and backfilling around a pile in periodic tides, the critical velocities (U_s, U_{snd}; U_b, U_{bnd}) can be written functionally as:

$$U_x = F(d_{50}, \rho_s, \rho, g, h, D, T, n) \tag{28}$$

where, U_x is a unified symbol for U_s, U_{snd}, U_b and U_{bnd}; F is the symbol of a function; d_{50} refers to the median diameter of the sediment particles; ρ_s and ρ are the density of sediment particle and water respectively; g is the acceleration of gravity; h is the mean water depth; D is the diameter of the pile; T is the tide period; n is the serial number of half cycles.

The U_{ini} in Fig. 15(b) represents the critical velocity for the initiation of sediment particle motion around a pile in unidirectional current. It serves as a significant reference for the initial value of U_x and should therefore be considered as an essential parameter in the function depicting the development of U_x. Similarly, U_{max} is also an essential parameter as it plays the role of upper limit of U_x before the equilibrium stage. In addition, the effects of tide period and serial number of half cycles on the development of U_x should vary across different cases. Therefore, the tide period T should be considered in a dimensionless form. Based on the previous studies (Sumer and Fredsoe, 2002), equation (28) can thereby be rewritten as:

$$U_x = F\left(U_{ini}, U_{max}, \frac{T}{T_s}, n\right) \tag{29}$$

where U_{ini} can be calculated by the following equations (Zhang, 2012). This empirical method was proposed based on the regression analysis of a large amount of onsite monitoring results and recommended by the a widely applied standard issued by MTPRC (2015) to estimate the U_{ini} of fine-grained bed.

$$U_{ini} = 0.645 \times \left(\frac{d_{50}}{D}\right)^{0.05} \times U_{cr} \tag{30}$$

$$U_{cr} = 1.34 \times \left(\frac{h}{D}\right)^{0.14} \left[(s-1)gd_{50} + 3.36 \times 10^{-7}\left(\frac{10+h}{d_{50}^{0.72}}\right)\right]^{0.5} \tag{31}$$

and the time scale T_s can be calculated by the following equations (Sumer and Fredsoe, 2002):

$$T_s = \frac{D^2}{\left[g(s-1)d_{50}^3\right]^{0.5}} T^* \tag{32}$$

$$T^* = \frac{1}{2000} \times \frac{h}{D} \times \theta^{-2.2} \tag{33}$$

where T_s and T^* are time scale and normalized time scale respectively. It should be note that the T_s calculated by equation (32) is not the real time scale for the scour progression of the tidal scenario. Instead, it represents the time scale for the corresponding unidirectional current scenario with a current velocity equivalent to the peak velocity of the tide. The value of $\frac{T}{T_s}$ reflects the development status of scour depth in each tide cycle. A higher value of $\frac{T}{T_s}$ indicates a greater change in scour depth in each half cycle, resulting in faster development of the U_x over n.

According to Soulsby (1997), the Shields parameter θ in equation (33) can be estimated by the following empirical equation:

$$\theta = \frac{U_f^2}{g(s-1)d} \tag{34}$$

where U_f is the undisturbed shear velocity.

Based on the data analysis of correlations between n and U_x of all sinusoidal tide scenarios, equation (29) is constructed in the form of an exponential function as:

$$U_x = (U_{max} - aU_{ini})\left\{1 - exp\left[b(n-1)\left(\frac{T}{T_s}\right)^c\right]\right\} + aU_{ini} \tag{35}$$

where a, b and c are coefficients.

In this study, the genetic-algorithm (GA) method is employed to search for the global optimal solution of coefficients in equation (29) based on the scour depth development data of all sinusoidal tide scenarios shown in Figss. 6–8. The fitness function of the GA method is constituted as:

$$G(a,b,c)=\frac{1}{M}\sum_{i=1}^{M}RMSE_i \tag{36}$$

$$RMSE_i=\sqrt{\frac{1}{N_i}\sum_{j=1}^{N_i}\left(U_{x,ij}-U'_{x,ij}\right)^2} \tag{37}$$

where $RMSE_i$ represents the root mean square error of calculated result in the *i-th* case, calculated by equation (37); M is the number of cases, herein the number of sinusoidal tide scenarios in this study is adopted; N_i is the number of half-cycles of the *i-th* case and is defined by $N_i = 2t_{endi}/T_i$, where t_{endi} and T_i are total scour time and the tide period of the *i-th* case respectively; $U_{x,ij}$ represents the calculated result of U_x in the *j-th* half-cycle of case *i*, while $U'_{x,ij}$ is the corresponding measured result.

The GA method in this study is implemented in a PYTHON script and the process can be generally summarized as follows.

(1) The coefficients a, b and c comprise the population.
(2) 100 initial populations are generated with random and various initial values of a, b and c.
(3) One case is selected, and U_x is calculated at each half-cycle of the selected case. The root mean square error of this case is then calculated using equation (37).
(4) Repeat step (3) to calculate the *RMSE* of each case and then employ equation (36) to calculate the value of $G(a,b,c)$, i.e., the mean *RMSE* value of all considered cases. The minimum value of $G(a,b,c)$ of all populations is adopted as the optimal fitness function result in the present iteration cycle.
(5) Update the population through the implementation of selection, crossover, and mutation; calculate the updated $G(a,b,c)$ of each new individual and update the optimal result of $G(a,b,c)$.
(6) Iterate step (3)–(5) until the optimal result of $G(a,b,c)$ reach a relatively low level and no longer varies significantly with iteration. Then the individual corresponding to the optimal $G(a,b,c)$ is identified as the global optimal solution of coefficients a, b and c. The global optimal values of coefficients a, b and c for U_s, U_{snd}, U_b and U_{bnd} of sinusoidal tide scenarios are summarized in Table 2.

6.3. Cumulative effective flow intensity based prediction method for equilibrium scour depth in periodic tides

Considering the prementioned limitation of effective flow work method, i.e., the variation of critical velocity with tide cycle is not considered, and the backfilling effect is neglected but the corresponding effective period is assumed to be positively corelated to scour depth growth. A new notion U_{int}, called the 'cumulative effective flow intensity', is proposed below for more accurately characterising the progression of scour pits in periodic tides. Referring to Fig. 15(b), the mathematical equation for U_{int} developing with time t is defined as:

$$U_{int}(t)=\int_0^t |U(t)|\delta(t)dt \tag{38}$$

where the Dirac–Delta function $\delta(t)$ is defined as follows:

$$\delta(t)=\begin{cases}1, & t\in(t_{si},t_{sndi})\\ -a, & t\in(t_{bi},t_{bndi})\\ 0, & t\notin[(t_{si},t_{sndi})\cup(t_{bi},t_{bndi})]\end{cases} \tag{39}$$

where t_{si}, t_{sndi}, t_{bi} and t_{bndi} are illustrated in Fig. 15(b) and represent the critical time points of the initialization and end of scouring and backfilling processes in each half cycle; a is an reduction coefficients. Through data analysis, it has been observed that the integration of flow velocity has a weaker effect on the backfilling process compared to the subsequent scouring process. The extent of reduction for this effect falls within the range of 0.2–0.6. In this study, a reduction coefficient of 0.45 is adopted.

Equation (39) delineates three distinct time periods within the current velocity signal of tides to compute the integration of flow velocity. The integration values of flow velocity during effective scouring periods, symbolized by the red shaded areas in Fig. 15(b), are considered positive, indicating their contribution to scour depth growth. Conversely, effective backfilling periods have negative effect on scour depth growth, and as a result, the negative integration values are adopted accordingly. Time periods not encompassed by these effective periods, having no impact on either scouring or backfilling, are excluded from the calculation of U_{int}.

The value of t_{si}, t_{sndi}, t_{bi} and corresponding U_{si}, U_{sndi}, U_{bi} represent the coordinates where the velocity signals intersect the critical velocity curves in Fig. 15(b). Accordingly, these critical values in each half cycle can be calculated by solving equation (35) combined with the current velocity signal function. It should be note that the current velocity signal refers to $|U(t)|$, i.e., the variation of current velocity magnitude with time. To elaborate, the value of U_{si}, U_{sndi}, U_{bi} in each half-cycle can be calculated using equation (35) with the coefficients listed in Table 2. Once these critical velocities (U_{si}, U_{sndi}, U_{bi}) are obtained, they are substituted into the current velocity magnitude signal function $|U(t)|$. Then a series of time points (t_{si}, t_{sndi}, t_{bi}) can be obtained.

In the case of symmetrical sinusoidal tide scenarios, as depicted in Fig. 15(b), the backfilling and scouring processes always convert at $t = t_{si}$, which is both the end of backfilling process and initiation of scouring process in the present half-cycle. Therefore, $t_{bndi} = t_{si}$ is adopted for the symmetrical sinusoidal tide scenarios. For asymmetrical sinusoidal tides characterized by different peak flow velocities in ebb and flow of tides, the value of t_{bndi} must be calculated differently. For half-cycles with calculated U_{si} and U_{sndi} lower than the corresponding peak flow velocity, the value of t_{bndi} is determined using the same method as for symmetrical sinusoidal tide scenarios. But when U_{si} or U_{sndi} is higher than the peak flow velocity in the corresponding half-cycle, the t_{bndi} is calculated by solving equation (35) combined with the absolute current velocity signal function $|U(t)|$. Specifically, the value of U_{sndi} in each half-cycle is calculated by the $U_{snd}(n)$ in equation (35) with the coefficients listed in Table 2. Once the U_{sndi} is obtained, it is then substituted into the $|U(t)|$ function to find the t_{bndi}.

If both U_{sndi} and U_{bndi} are higher than the peak velocity in the corresponding half-cycle, or if the variation of U_{int} in one complete tide cycle decreases to 0, it is suggested that the equilibrium stage has been reached. The corresponding equilibrium time t_{eq} can be calculated by:

$$t_{eq}=2n_{eq}T \tag{40}$$

where T is the tide period; n_{eq} is the number serial of half-cycles after which the equilibrium stage is reached.

Then the cumulative effective flow intensity of sinusoidal tide before the equilibrium stage is normalized by the flow intensity of corresponding unidirectional current with a current velocity equivalent to the maximum tidal velocity. Accordingly, the normalized cumulative effective flow intensity f_t is defined as:

$$f_t=\frac{\int_0^{t_{eq}}|U(t)|\delta(t)dt}{U_{max}t_{eq}} \tag{41}$$

The sinusoidal tide, which closely resembles the realistic pattern of tides, always lead to a lower equilibrium scour depth compared to unidirectional current with a velocity equivalent to the maximum tidal velocity. This indicates that the equilibrium scour depth induced by sinusoidal tide S_T could be estimated through multiplying a ratio coefficient K_T by the equilibrium scour depth induced by corresponding unidirectional current S_c (Schendel et al., 2018; Wang et al., 2024).

The equilibrium scour depth for all sinusoidal tide scenarios in this study, along with scour data from (Schendel et al., 2018), are collected, and the ratio coefficient ($K_T = S_T/S_c$) is plotted in Fig. 16 against the

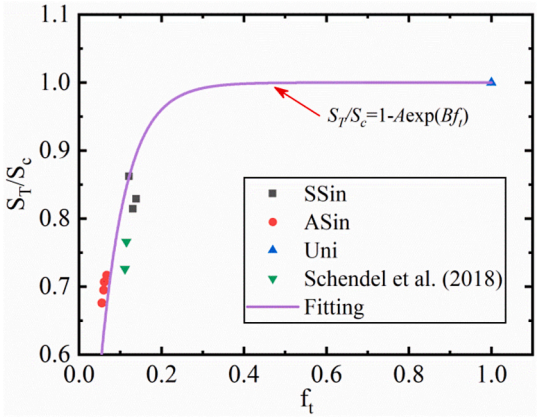

Fig. 16. Correlation between ratio of equilibrium scour depth produced by tide S_T and corresponding unidirectional current S_c with normalized cumulative effective flow intensity f_t.

normalized cumulative effective flow intensity f_t. Despite the variation in tide periods, all data points for SSin in Fig. 16 show similar f_t and S_T values. Similar phenomenon can be observed from the data points of ASin in Fig. 16.

According to the definition of cumulative effective flow intensity, SSin scenarios exhibit longer effective scouring periods compared to the ASin scenarios. This is primarily due to the lower current velocities observed during the weaker half-cycles of ASin scenarios. Consequently, as can be observed in Fig. 16, the f_t values for SSin scenarios are always higher than those for ASin scenarios. This leads to higher S_T values for SSin scenarios, indicating that the equilibrium scour depth is primarily determined by the normalized cumulative effective flow intensity. Fig. 16 shows that tide period has less effect on f_t, which explains the prementioned phenomenon that tide periods have less effect on equilibrium scour depth compared to the tide patterns.

Fig. 16 illustrates that K_T gradually increases with f_t and progressively approaches 1.0 at $f_t = 1.0$, which represents the unidirectional current scenarios. It is reasonable to infer that the value of K_T at $f_t = 0$ should be 0, considered as the lower boundary of the estimation correlation function between K_T and f_t. Based on the data points plotted in Fig. 16, an empirical equation is proposed to depict the correlation between K_T and f_t, as follows:

$$K_T = \frac{S_T}{S_c} = 1 - A\exp(Bf_t) \tag{42}$$

where A = 0.951 and B = −15.869 is obtained based on the nonlinear fitting results of data points in Fig. 16.

Based on equation (42), the equilibrium scour depth induced by periodic tides can be calculated once the scour depth induced by the corresponding unidirectional current is measured or calculated using widely applied methods such as HEC-18 method (Richardson and Davis, 1995) and the revised 65-1 formula (MTPRC, 2015). Herin the current velocity of the unidirectional current is equivalent to the maximum current velocity of corresponding periodic tide. It should be noted that when a measured S_c is not available, the calculated S_c may slightly vary depending on the selected formula. The calculation method for S_c should

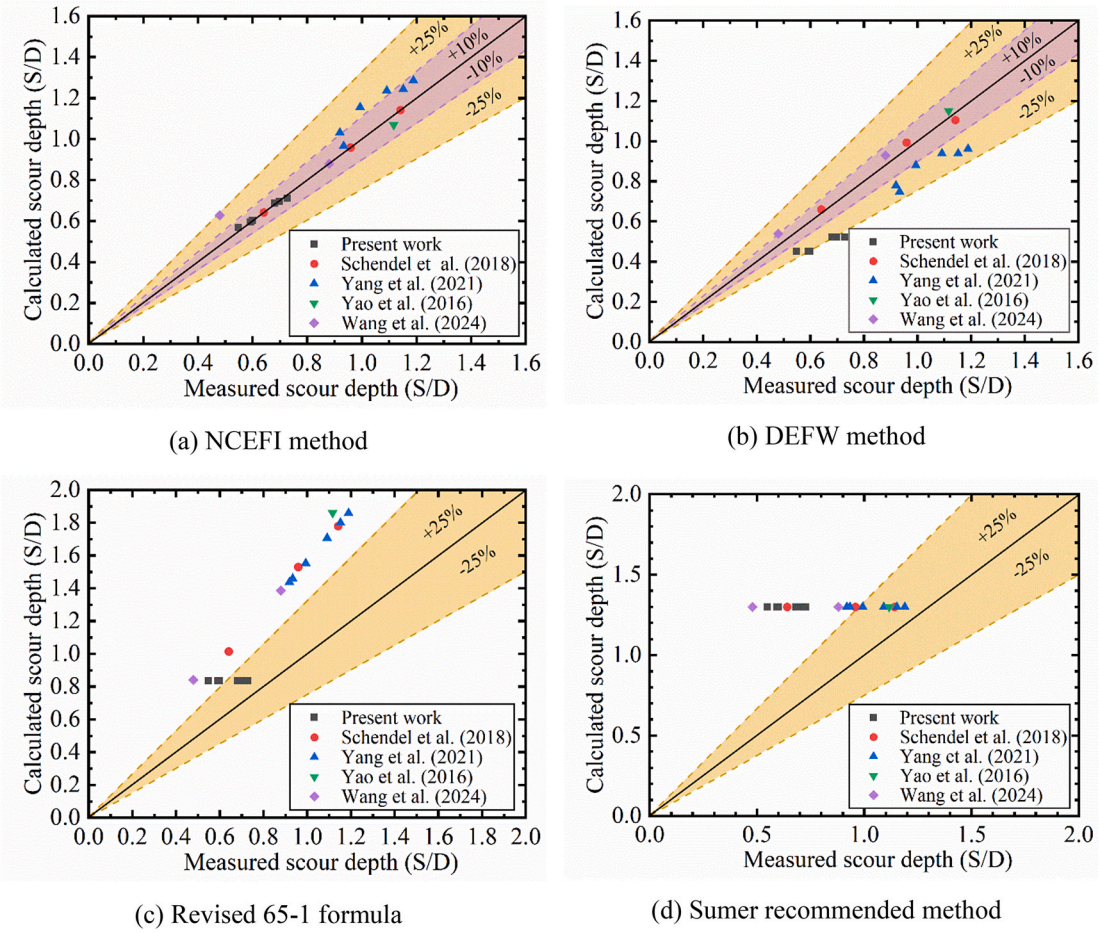

Fig. 17. Comparison of measured scour depth and results calculated by: (a) Normalized cumulative effective flow intensity method; (b) Dimensionless effective flow work method (Schendel et al., 2019; Wang et al., 2024); (c) Revised 65-1 formula (MTPRC, 2015); (d) Sumer recommended method (Sumer and Fredsoe, 2002).

be decided based on the onsite hydraulic and geological conditions and standard recommendations (Richardson and Davis, 1995; MTPRC, 2015; DNV, 2016).

In this study, the normalized cumulative effective flow intensity (NCEFI) method is applied to predict the scour depths for all sinusoidal tide scenarios, with the results illustrated in Fig. 17 (a). To verify the prediction accuracy and generalization capability of this method, scour data reported in previous studies (Yao et al., 2016; Schendel et al., 2018; S. Yang et al., 2021; Wang et al., 2024) are also plotted in Fig. 17 (a) along with the calculated results of the NCEFI method. It should be note that not all the experimental data from these studies are incorporated in Fig. 17. As explained above that the NCEFI method predicts S_T based on S_c. Fig. 17 is plotted to verify the accuracy and generalization capability of NCEFI method (as defined by Equation (42). Therefore, this figure includes only data from previous studies that provide corresponding unidirectional current-induced scour measurements. Data sets lacking these specific measurements have been excluded to ensure a fair assessment of the method's performance.

In addition to the NCEFI method, the calculation results using the prementioned DEFW method (Schendel et al., 2019; Wang et al., 2024), the revised 65-1 formula (MTPRC, 2015) and the Summer method (Sumer and Fredsoe, 2002) are plotted in Fig. 17 (b)–(d) respectively, to compare the prediction accuracy of these methods.

As shown in Fig. 17 (c) the revised 65-1 formula exhibits a calculation error of more than 25%. This formula is based on onsite measured scour data from bridges constructed across rivers, which are rarely affected by periodic tides. The backfilling process is not considered in this method, resulting in an over-estimation of scour depth in periodic tides. The Sumer method considered the backfilling effects in oscillator flow induced by waves, using the Keulegan–Carpenter number to calculate the scour depth. However, the Keulegan–Carpenter number for tides is much higher than waves, and consequently, the calculated S_T is equivalent to S_c, which is assumed to be $1.3D$ in this method. Consequently, the calculated results of the Sumer method, illustrated in Fig. 17 (d), deviate significantly from the measured data. In contrast, the NCEFI and DEFW methods are specifically designed for predicting scour depth induced by periodic tides, and both exhibit high prediction accuracy. As illustrated in Fig. 17 (a) and (b), most data points of NCEFI and DEFW fall within the 10% error line, suggesting that both methods have significant potential for application in predicting tides induced scour depth.

6.4. Prediction of scour depth development process in periodic tides

Despite the effective flow work method exhibits good performance in predicting the equilibrium scour depth induced by tides, it lacks the capability to calculate the development progression of scour depth due to the neglect of effective backfilling periods and variations in critical velocities with tide cycles in the calculation of effective flow work. In this study, this limitation is addressed by utilizing the cumulative effective flow intensity, as calculated by equation (38), to predict the maximum scour depth development progressions induced by periodic tides.

Equation (38) shows that U_{int} varies with time. The previous section explained the calculation process of the equilibrium time point t_{eq}, based on which the U_{int} at $t = t_{eq}$ can be calculated. The development of maximum scour depth corresponds to the variation in U_{int} over time. Assuming a consistent trend between the development of maximum scour depth and U_{int}, a prediction formula for scour depth progression can be established as, in which the maximum scour depth is represented as a function of time.

$$S(t) = \frac{U_{int}(t)}{U_{int}(t_{eq})} S_T \tag{43}$$

where $S(t)$ represents the maximum scour depth at time t; S_T denotes the equilibrium scour depth calculated by equation (42); $U_{int}(t)$ and $U_{int}(t_{eq})$ are calculated by equation (38) and refer to the cumulative effective flow intensity at time t and at the equilibrium stage respectively.

In this study, equation (43) is applied to predict the scour depth development progressions of cases presented in Fig. 17. Part of the predicted results are plotted in Fig. 18 along with the measured data for comparison. Each subplot in Fig. 18 illustrates a high degree of consistency between the calculated and observed scour progressions, indicating that equation (43) captures not only the overall development trend but also almost all the increase-suspension-decrease periods, even when the fluctuation is minor. However, there are instances of relative underestimation in the scour depth for symmetrical sinusoidal tides, particularly in the initial 1–2 cycles, followed by a slight overestimation of scour depth fluctuation in the subsequent cycles, as evidenced in Fig. 18 (a) and (c)–(f). Asymmetrical tide scenarios show an overall overestimation of scour depth fluctuation throughout the scour progression, as illustrated in Fig. 17 (b). The under or over estimation of the scour depth fluctuation can be attributed to the assumption underlying equation (43) that the development trends of maximum scour depth and U_{int} with time are consistent. In fact, the effect of variation of U_{int} on scouring or backfilling may slightly vary with time, though the variation trend is presently not clear.

In this study, the U_{int} calculated by equation (38) stabilizes after reaching the equilibrium stage, and consequently, the scour depth predicted by equation (43) also stabilize thereafter. However, Fig. 18 (a)–(c) reveal that while the predicted scour depths remain constant in the last several cycles, the measured data still exhibit slight variation. This observation suggests that that the equilibrium stage predicted by the effective flow intensity method may be slightly earlier than indicated by the measured data.

Despite its effective performance in predicting both equilibrium scour depth and scour progression under sinusoidal-like tidal conditions, the cumulative effective flow intensity method has some limitations. Specifically, equation (35) cannot be applied to estimate the characteristic time points (i.e. t_{si}, t_{sndi}, t_{bi} and t_{bndi}) in square tides scenarios, as there are no intersections between curves derive from equation (35) and current velocity signals of square tides scenarios. Therefore, the prediction method proposed in this study is only applicable to sinusoidal-like tides with time-varying flow velocities and cannot applied to the square tide scenarios. In addition, since this method is based on experimental and numerical data, further validation through onsite studies is imperative before it can be confidently applied in engineering practice.

7. Conclusions

To develop a method for predicting the progression of scour depth around monopile foundations in tidal ebb and flow, this paper presents a comprehensive study and establishes a reliable numerical model. The study investigates the combined impact of tide patterns, tidal periods, and the symmetry and asymmetry of tides on scour formation. The results enhance the understanding of scour in periodic tidal conditions and introduce a novel prediction method. Specifically, the following conclusions can be drawn.

- The varying impacts of the ebb and flow of periodic tides on scouring and backfilling cause fluctuations in the growth of the maximum scour depth, particularly during the initial stages. However, as the scour depth increases, these fluctuations gradually diminish due to the additional damping effect of the water in the scour pit, which weakens the influence of vortices.
- From the perspective of cumulative effective flow intensity, square tides have the potential to cause the most severe scour around monopiles, followed by symmetric sinusoidal tides. However, unlike these two types, asymmetric sinusoidal tides, which more closely resemble real-life tidal conditions, result in the weakest scour around

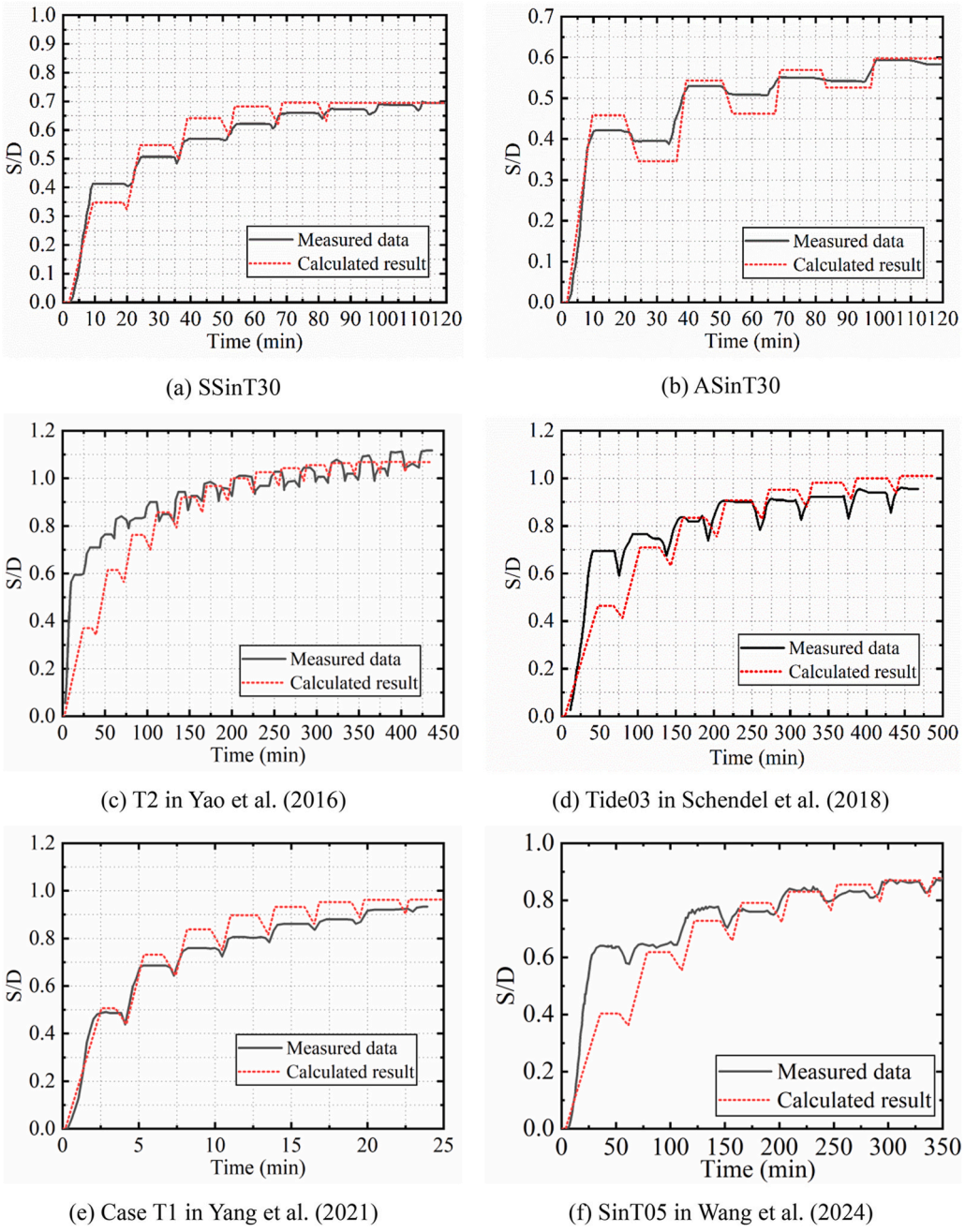

Fig. 18. Comparisons of scour depth development progression, plotted based on measured data and calculated results for various scenarios: (a) Case SSinT30 in present study; (b) Case ASinT30 in present study; (c) Case T2 in (Yao et al., 2016); (d) Case Tide03 in (Schendel et al., 2018); (e) Case T1 in (S. Yang et al., 2021); (f) Case SinT05 in (Wang et al., 2024).

monopiles. Consequently, offshore wind turbine (OWT) foundations may face reduced scouring risks in the ebb and flow of tides compared to unidirectional tidal currents, due to the backfilling effect of the reverse flow.

- The tidal period can significantly affect the time scales of scour development, with longer periods accelerating the progression of scour. However, it has minimal impact on the equilibrium scour depth. This is attributed to the similarity in normalized effective flow intensities across tides with the same patterns, regardless of variations in tidal periods.
- In square and sinusoidal tides, the scour depths at the front and back sides of the pile exhibit symmetry, whereas asymmetrical tides can result in asymmetric scour pits akin to those induced by unidirectional currents.
- A new concept named cumulative effective flow intensity is proposed in this study, with the variability of critical velocities throughout tide cycles being taken into account. The effects of both effective scouring and backfilling periods are considered. It is highlighted by the findings that the cumulative effective flow intensity is a primary factor governing equilibrium scour depth in tidal scenarios.
- Based on the correlation analysis between normalized cumulative effective flow intensity of tides and equilibrium scour depth, an empirical formula is proposed to predict the equilibrium scour depth in sinusoidal tides. The formula demonstrates a high level of accuracy, fitting well with data from both this study and previous studies.
- By considering the time-varying cumulative effective flow intensity and the calculated equilibrium scour depth, a prediction method for the development progression of scour depth under sinusoidal tides is

proposed. The accuracy of this method is validated by experimental data from the literature.

It is worth noting that all the conclusions drawn in this study are based on simulation results from scaled numerical models. The experimental data adopted to validate the prediction method were also obtained from scaled model tests. Therefore, considering the potential scale effects, onsite validation is essential before these methods can be confidently applied to real-world conditions in the future.

CRediT authorship contribution statement

Fei Geng: Writing – review & editing, Writing – original draft, Visualization, Validation, Methodology, Investigation, Funding acquisition. **Wenxian Yang:** Writing – review & editing, Supervision, Conceptualization. **Sadegh Nadimi:** Writing – review & editing, Supervision. **Zhiqiang Hu:** Writing – review & editing, Supervision.

Declaration of competing interest

The authors declare that they have no known competing financial interests or personal relationships that could have appeared to influence the work reported in this paper.

Acknowledgements

The work reported above was supported by China Scholarship Council (CSC) with the reference number of 202106220076.

References

Breusers, H.N.C., Nicollet, G., Shen, H.W., 1977. Local scour around cylindrical piers. J. Hydraul. Res. 15 (3), 211–252. https://doi.org/10.1080/00221687709499645.

Carreiras, J., Larroudé, P., Seabra-Santos, F., Mory, M., 2012. Wave Scour Around Piles 1860–1870. https://doi.org/10.1061/40549(276)145.

Chreties, C., Teixeira, L., Simarro, G., 2013. Influence of flow conditions on scour hole shape for pier groups. In: Proceedings of the Institution of Civil Engineers-Water Management. Thomas Telford Ltd, pp. 111–119.

Dai, S., Han, B., Wang, B., Luo, J., He, B., 2021. Influence of soil scour on lateral behavior of large-diameter offshore wind-turbine monopile and corresponding scour monitoring method. Ocean Eng. 239, 109809 https://doi.org/10.1016/j.oceaneng.2021.109809.

DNV, (Det Norske Veritas), 2016. Support structures for wind turbines. Høvik, Norway. Det Norske Veritas AS. https://www.dnv.com/energy/standards-guidelines/dnv-st-0126-support-structures-for-wind-turbines/. Accessed: 20 May 2024.

Escarameia, M., May, R., 1999. Scour Around Structures in Tidal Flows. HR Wallingford, UK.

Geng, F., Yang, W., Nadimi, S., Han, B., Huang, G., 2023. Study for predicting the earthquake-induced liquefaction around the monopile foundation of offshore wind turbines. Ocean Eng. 268, 113421 https://doi.org/10.1016/j.oceaneng.2022.113421.

Gunnar, H., 2022. Global Offshore Wind Report 2021. World Forum Offshore Wind, Hamburg.

Jensen, M.S., Larsen, B.J., Frigaard, P., Vos, L.D., Bove, S., 2006. Offshore Wind Turbines Situated in Areas with Strong Currents, 6004RE01ER1. Offshore Centre Denmark.

Kadivar, M., Tormey, D., McGranaghan, G., 2021. A review on turbulent flow over rough surfaces: fundamentals and theories. International Journal of Thermofluids 10, 100077. https://doi.org/10.1016/j.ijft.2021.100077.

Lee, J., Zhao, F., 2021. Global Offshore Wind Report 2021. Global Wind Energy Council, Brussels.

Link, O., Castillo, C., Pizarro, A., Rojas, A., Ettmer, B., Escauriaza, C., Manfreda, S., 2017. A model of bridge pier scour during flood waves. J. Hydraul. Res. 55 (3), 310–323. https://doi.org/10.1080/00221686.2016.1252802.

Margheritini, L., Martinelli, L., Lamberti, A., Frigaard, P., 2007. Scour around monopile foundation for off-shore wind turbine in presence of steady and tidal currents. In: Coastal Engineering 2006. World Scientific Publishing Company, pp. 2330–2342.

Mastbergen, D.R., Van Den Berg, J.H., 2003. Breaching in fine sands and the generation of sustained turbidity currents in submarine canyons. Sedimentology 50 (4), 625–637. https://doi.org/10.1046/j.1365-3091.2003.00554.x.

McGovern, D., Ilic, S., Folkard, A.M., McLelland, S.J., Murphy, B.J., 2014. Time development of scour around a cylinder in simulated tidal currents. J. Hydraul. Eng. 140 (6), 04014014 https://doi.org/10.1061/(ASCE)HY.1943-7900.0000857, 04014014.

Melville, B.W., Raudkivi, A.J., 1977. Flow characteristics in local scour at bridge piers. J. Hydraul. Res. 15 (4), 373–380. https://doi.org/10.1080/00221687709499641.

Meyer-Peter, E., Müller, R., 1948. Formulas for bed-load transport. In: Proceedings of the 2nd Meeting of the International Association for Hydraulic Structures Research, pp. 39–64.

MTPRC, (Ministry of Transport of the People's Republic of China), 2015. Hydrological Specifications for Survey and Design of Highway Engineering. Industry Standard-Transportation, Beijing, China.

Ong, M.C., Myrhaug, D., Hesten, P., 2013. Scour around vertical piles due to long-crested and short-crested nonlinear random waves plus a current. Coast Eng. 73, 106–114. https://doi.org/10.1016/j.coastaleng.2012.10.005.

Petersen, T.U., Sumer, B.M., Fredsøe, J., 2012. Time scale of scour around a pile in combined waves and current. In: International Conference on Coastal Engineering, p. 8.

Pizarro, A., Ettmer, B., Manfreda, S., Rojas, A., Link, O., 2017. Dimensionless effective flow work for estimation of pier scour caused by flood waves. J. Hydraul. Eng. 143 (7), 06017006 https://doi.org/10.1061/(ASCE)HY.1943-7900.0001295.

Porter, K.E., Simons, R.R., Harris, J.M., 2014. Laboratory investigation of scour development through a spring-neap tidal cycle. In: Proceedings of the 7th International Conference on Scour and Erosion, pp. 2–4. https://doi.org/10.1201/b17703-87. Perth, Australia.

Qi, W., Gao, F., 2014a. Equilibrium scour depth at offshore monopile foundation in combined waves and current. Sci. China Technol. Sci. 57 (5), 1030–1039. https://doi.org/10.1007/s11431-014-5538-9.

Qi, W.-G., Gao, F.-P., 2014b. Physical modeling of local scour development around a large-diameter monopile in combined waves and current. Coast Eng. 83, 72–81. https://doi.org/10.1016/j.coastaleng.2013.10.007.

Qin, B., Xie, Y., Yang, W., Qu, R., Geng, F., 2023. A further study on the scour around the monopile foundation of offshore wind turbines. Sustain. Energy Technol. Assessments 57, 103198. https://doi.org/10.1016/j.seta.2023.103198.

Richardson, E.V., Davis, S.R., 1995. Evaluating Scour at Bridges. Federal Highway Administration. Office of Technology Applications, United States. https://rosap.ntl.bts.gov/view/dot/1024. Accessed: 14 March 2024.

Roulund, A., Sumer, B.M., Fredsøe, J., Michelsen, J., 2005. Numerical and experimental investigation of flow and scour around a circular pile. J. Fluid Mech. 534, 351–401. https://doi.org/10.1017/S0022112005004507.

Salaheldin, T.M., Imran, J., Chaudhry, M.H., 2004. Numerical modeling of three-dimensional flow field around circular piers. J. Hydraul. Eng. 130 (2), 91–100. https://doi.org/10.1061/(ASCE)0733-9429(2004)130:2(91).

Schendel, A., Hildebrandt, A., Goseberg, N., Schlurmann, T., 2018. Processes and evolution of scour around a monopile induced by tidal currents. Coast Eng. 139, 65–84. https://doi.org/10.1016/j.coastaleng.2018.05.004.

Schendel, A., Welzel, M., Hildebrandt, A., Schlurmann, T., Hsu, T.-W., 2019. Role and impact of hydrograph shape on tidal current-induced scour in physical-modelling environments. Water 11 (12), 2636. https://doi.org/10.3390/w11122636.

Soulsby, R., 1997. Dynamics of Marine Sands. Thomas Telford Ltd. http://www.icevirtuallibrary.com/content/book/100318. Accessed: 28 November 2023.

Sumer, B.M., Fredsoe, J., 2002. The mechanics of scour in the marine environment. World Scientific.

Wang, S.-Y., Qi, W.-G., Li, B., Wang, C., Gao, F.-P., 2024. Tidal currents-induced scour development around pile foundations: effects of flow velocity hydrograph. Coast Eng. 191, 104533 https://doi.org/10.1016/j.coastaleng.2024.104533.

Whitehouse, R.J.S., Harris, J.M., Sutherland, J., Rees, J., 2011. The nature of scour development and scour protection at offshore windfarm foundations. Mar. Pollut. Bull. 62 (1), 73–88. https://doi.org/10.1016/j.marpolbul.2010.09.007.

Whitehouse, R.J.S., Stroescu, E.I., 2023. Scour depth development at piles of different height under the action of cyclic (tidal) flow. Coast Eng. 179, 104225 https://doi.org/10.1016/j.coastaleng.2022.104225.

Yakhot, V., Orszag, S.A., Thangam, S., Gatski, T.B., Speziale, C.G., 1992. Development of turbulence models for shear flows by a double expansion technique. Phys. Fluid. Fluid Dynam. 4 (7), 1510–1520. https://doi.org/10.1063/1.858424.

Yang, B., Wei, K., Yang, W., Li, T., Qin, B., 2021a. A feasibility study of reducing scour around monopile foundation using a tidal current turbine. Ocean Eng. 220, 108396 https://doi.org/10.1016/j.oceaneng.2020.108396.

Yang, S., Xia, Y., Wang, S., 2021b. Local scour around a monopile in reciprocating tidal current considering the effect of water depth. J. Phys. Conf. 1834 (1), 012019 https://doi.org/10.1088/1742-6596/1834/1/012019.

Yao, W., An, H., Draper, S., Cheng, L., Zhao, M., Jesudoss, J.S., Tang, G., 2016. Experimental study of local scour around piles in tidal currents. In: 20th Australasian Fluid Mechanics Conference, pp. 5–8. Perth, Australia.

Zhang, H., 2012. A unified formula for incipient velocity of sediment. J. Hydraul. Eng. 43 (12), 1387–1396.

Zhang, W., Cao, Y., Zhu, Y., Zheng, J., Ji, X., Xu, Y., Wu, Y., Hoitink, A.J.F., 2018. Unravelling the causes of tidal asymmetry in deltas. J. Hydrol. 564, 588–604. https://doi.org/10.1016/j.jhydrol.2018.07.023.